

1     **Stratospheric versus Tropospheric Control of the Strength and**  
2             **Structure of the Brewer-Dobson Circulation**

3                     EDWIN P. GERBER \*

*Center for Atmosphere Ocean Science,*

*Courant Institute of Mathematical Sciences, New York University, New York NY*

Submitted for publication in the Journal of the Atmospheric Sciences,  
December, 2011.

---

\* *Corresponding author address:* Edwin P. Gerber, Center for Atmosphere Ocean Science, Courant Institute of Mathematical Sciences, 251 Mercer Street, New York NY 10012.

E-mail: gerber@cims.nyu.edu

## ABSTRACT

4  
5 The strength and structure of the Brewer-Dobson Circulation (BDC) are explored in an ide-  
6 alized General Circulation Model. It is shown that the diabatic forcing of the stratosphere  
7 and planetary wave forcing by the troposphere have comparable effects on mass transport  
8 through the stratosphere, as quantified by the mean age of air and age spectrum. Their  
9 impact on the transport, however, is mediated through different controls on the residual, or  
10 isentropic circulation. Planetary waves are modulated by changing surface topography. In-  
11 creased planetary wave forcing strengthens the isentropic circulation, particularly the lower  
12 branch. This is primarily a tropospheric control on the BDC, as the wave forcing is set by  
13 stationary waves at the base of the stratosphere. Stratospheric control on the circulation is  
14 effected indirectly through the strength of the stratospheric polar vortex. A colder vortex  
15 creates a waveguide higher into the stratosphere, raising the breaking level of the Rossby  
16 waves and deepening the circulation. Ventilation of mass in the stratosphere depends crit-  
17 ically on the depth of tropical upwelling, and so transport is comparably sensitive to both  
18 tropospheric and stratospheric controls.

19 The two controls on the strength and depth of the circulation can lead to separate  
20 influences on the lower and upper stratosphere. It is possible to observe independent changes  
21 in the “shallow” and “deep” circulations, which may be important for comparing modeled  
22 trends of the BDC with observations. It is also shown that changes in the BDC can increase  
23 the equator-to-pole gradient in tropopause height by up to two kilometers, and cool the  
24 tropical cold point by up to 1.5 Kelvin.

# 1. Introduction

The Brewer-Dobson Circulation (BDC) characterizes the transport of mass through the stratosphere, a slow upwelling in the tropics, poleward drift through the midlatitudes, and descent over the poles. Dobson et al. (1929) first speculated on the existence of this transport based on the positive equator-to-pole gradient in stratospheric ozone in the boreal spring, a gradient seemingly at odds with the (then) hypothesis that ozone is produced by solar radiation. Unfortunately the conjecture was initially abandoned, and it was not until further measurements of water vapor and helium by Brewer (1949) that sufficient evidence was established. In concert with radiative and chemical processes, the Brewer-Dobson Circulation sets the distribution of ozone and water vapor in the middle atmosphere (e.g. Dobson 1956). Stratospheric ozone changes have played an order one role in observed circulation trends to date, shifting the tropospheric jet stream in the Southern Hemisphere (e.g. Thompson and Solomon 2002; Arblaster and Meehl 2006; Polvani et al. 2011). Likewise, Solomon et al. (2010) show that changes in stratospheric water vapor have had a significant impact on observed surface warming. Understanding and simulating the BDC is thus critical for interpreting changes in stratospheric water vapor and ozone in recent decades, and will continue to be so for projections of future climate (e.g. Perlwitz et al. 2008; Son et al. 2008; McLandress et al. 2011).

In this paper, we study the factors that control the strength and structure of the Brewer-Dobson Circulation, focussing on the joint roles of the stratosphere and troposphere in shaping mass transport in the stratosphere. To build a bridge between conceptual models of the BDC (e.g. Dunkerton 1989; Holton et al. 1995) and comprehensive simulations with stratosphere resolving atmospheric models (e.g. McLandress and Shepherd 2009), we study the transport in an idealized General Circulation Model. The model, developed by Polvani and Kushner (2002) and Gerber and Polvani (2009), simulates the primitive equation dynamics of the atmosphere with the same fidelity as comprehensive models, therefore capturing the nonlinear interactions between planetary and synoptic waves with the mean

52 flow, but with an idealized forcing that allows us to systematically vary both tropospheric  
53 and stratospheric conditions. A key conclusion of our study is that both tropospheric wave  
54 forcing and stratospheric diabatic forcing can have equal impact on mass transport in the  
55 middle to upper stratosphere.

56 The extremely long time scales of the BDC, on the order of years for much of the strato-  
57 sphere, prohibit direct measurement of the circulation. In addition, the Lagrangian circu-  
58 lation outside the deep tropics is primarily effected by eddies, and so best quantified by  
59 the residual mean circulation of the Transformed Eulerian Mean (TEM) equations (Edmon  
60 et al. 1980; Andrews et al. 1987). As established in the downward control principle by  
61 Haynes et al. (1991), the circulation outside of the deep tropics is mechanically driven by  
62 wave induced torques. Downward control allows one to estimate the Lagrangian mean cir-  
63 culation indirectly from the heating generated by vertical motion – which can be estimated  
64 from direct measurements – and so provides a means for quantifying the observed BDC (e.g.  
65 Rosenlof 1995). As discovered by Brewer (1949) and Dobson (1956), however, the BDC  
66 is fundamentally connected to the transport of chemical species. The estimate of the La-  
67 grangian transport in the TEM circulation captures the isentropic circulation, that is, the  
68 transport of mass across isentropic surfaces, but does not account for the mixing of mass  
69 along isentropes (e.g. Plumb 2002). Mass transport by the BDC is therefore more directly  
70 related to tracer based metrics, in particular the mean age of air and age spectrum (Waugh  
71 and Hall 2002). These measures quantify the length and variability of transport pathways  
72 through the stratosphere.

73 To connect tracer transport to the Lagrangian circulation, we compare tracer based  
74 calculations of the age spectrum with the residual mean circulation. We probe the impact  
75 of changes in the tropospheric wave forcing on the BDC by altering the surface orography of  
76 the model, and the impact of changes of the diabatic forcing in the stratosphere by varying  
77 the cooling of the winter polar vortex. As would be expected from downward control theory,  
78 increased planetary wave forcing increases the amplitude of the residual mean circulation.

79 Tracer transport follows the circulation changes, and the mean, modal, and spectral width of  
80 the age spectrum decrease. We term the impact of the planetary wave forcing “tropospheric  
81 control” of the BDC, as it is largely independent of stratospheric conditions. Given that  
82 the BDC is entirely mechanically forced, however, the impact of diabatic forcing in the  
83 stratosphere is less intuitive. The structure of the polar vortex has relatively little impact on  
84 the net isentropic transport into and out of the stratosphere, but controls the distribution  
85 of wave breaking, and so the depth of the residual circulation. In terms of tracer transport,  
86 however, this has an equally important impact on the age spectrum statistics in the mid  
87 to upper stratosphere. We term this influence of stratospheric conditions “stratospheric  
88 control” of the BDC, as it is largely independent of the planetary wave forcing from the  
89 troposphere below.

90 In studying the circulation with an idealized GCM, we have omitted the impact of small  
91 (10-1000 km) scale gravity waves. Such “unresolved” gravity waves play a significant role in  
92 stratospheric circulation, driving roughly 10-25% of the stratospheric circulation in compre-  
93 hensive models (e.g. Eyring et al. 2010, Chpt. 4). We have chosen to focus on the resolved  
94 circulation in this study to establish a reproducible, conceptual framework. As gravity waves  
95 are the primary driver of the circulation in the mesosphere, we focus only on the stratospheric  
96 circulation, where resolved waves dominate. Future work will explore the impact of gravity  
97 wave parameterizations in the idealized GCM. Initial tests have suggested, however, that  
98 there is a substantial degree of compensation between resolved and parameterized waves.

99 While not the primary focus of this paper, several recent studies have investigated changes  
100 in the BDC in response to anthropogenic forcing. Comprehensive models universally predict  
101 an increase of the circulation (e.g. Butchart and Scaife 2001; Li et al. 2008; Garcia and  
102 Randel 2008; McLandress and Shepherd 2009). Observational evidence is less conclusive;  
103 Engel et al. (2009) suggest the transport may actually be decreasing, but the uncertainty in  
104 measurements is sufficiently large that model trends cannot be ruled out (e.g. Garcia et al.  
105 2011). Our results may have bearing on the changes, however, in light of the conjecture by

106 Bönisch et al. (2011) that differences between observations and models could be related to  
107 structural changes in the BDC. Our idealized model integrations confirm that such structural  
108 changes in the circulation are possible, illustrating that transport in the lower stratosphere,  
109 the “lower branch” of the BDC, can vary independently of the “upper branch” of transport  
110 in the middle to upper stratosphere.

111 In Section 2, we describe the model and introduce the key diagnostics of the paper, the  
112 mean age of air, age spectrum, and residual mean circulation. Section 3 presents the key  
113 result of the paper, highlighting the difference between tropospheric and stratospheric control  
114 of the Brewer-Dobson Circulation. This conceptual framework is developed in detail in  
115 sections 4 and 5, where we explore the impact of model parameters on the residual circulation  
116 and connect these changes to the mass transport, respectively. Potential impacts of the  
117 BDC on climate are presented in Section 6, where we focus on changes in the tropopause  
118 and tropical cold point. Lastly, we summarize our results and place them in the context of  
119 potential anthropogenic influences on the BDC in Section 7.

## 120 **2. Model and Methods**

121 A series of perpetual January integrations with an idealized General Circulation Model  
122 (GCM) form the core of the study. The runs are nearly identical to those presented in  
123 Gerber and Polvani (2009). The model is a pseudo-spectral dynamical core developed by  
124 the Geophysical Fluid Dynamics Laboratory (GFDL) and forced with a highly simplified  
125 physical parameterization, as described by Held and Suarez (1994) and modified by Polvani  
126 and Kushner (2002) to produce a realistic circulation in the stratosphere and troposphere.  
127 We refer the reader to these papers for the precise details of the forcing, but review the most  
128 important features here.

129 The key simplification to the model physics is in the temperature equation, where all  
130 diabatic processes are approximated by Newtonian relaxation to an analytic, radiative-

131 convective equilibrium-like profile. This allows the model to produce a fairly realistic mean  
132 circulation without radiation or convection schemes. In the troposphere, the profile is ex-  
133 actly as in Held and Suarez (1994), but that a gradient in temperature is introduced between  
134 the two hemispheres to mimic solsticial conditions. In the stratosphere, temperature in the  
135 summer hemisphere and tropics is relaxed to the U.S. Standard Atmosphere. In the winter  
136 hemisphere, a polar night jet is forced by reducing the temperature of the equilibrium profile.  
137 Over the polar cap, the equilibrium profile decreases in height with specified lapse rate  $\gamma$   
138  $\text{K km}^{-1}$ . The vortex lapse rate  $\gamma$  is a key parameter in this study. As it is increased, the  
139 winter stratosphere grows colder and polar vortex becomes stronger.

140 The second key variable in this study is the surface topography. As only planetary scale  
141 waves extend into the stratosphere (e.g. Charney and Drazin 1961), Gerber and Polvani  
142 (2009) showed that a very simple surface topography was sufficient to excite an active strato-  
143 spheric circulation. Surface topography of wavenumber  $k$  and amplitude  $h_0$  is added in the  
144 winter hemisphere between 25 and 65°N. Gerber and Polvani (2009) found that the most  
145 realistic stratosphere-troposphere coupling was found in simulations with  $\gamma = 4$  and topo-  
146 graphic wavenumber  $k = 2$  and amplitude  $h_0 = 3$  km.

147 The Polvani and Kushner (2002) GCM includes a crude parameterization of mesospheric  
148 gravity wave drag by introducing a Rayleigh friction above 0.5 hPa, acting on the 5 upper-  
149 most layers of the model, which extend to approximately 0.01 hPa. Drag near the model top  
150 is necessary to slow down the polar night jet, as the winds in radiative equilibrium exceed  
151 several hundred  $\text{ms}^{-1}$  at these altitudes. This crude parameterization, however, introduces  
152 a non-conservative drag in the uppermost atmosphere. Shepherd and Shaw (2004) show  
153 that this can effect the stratospheric and tropospheric circulations through downward con-  
154 trol. The negative effects are most pronounced in “low top” models with an upper boundary  
155 within the stratosphere, e.g. 10 hPa, as documented by Shaw et al. (2009). Aware of this po-  
156 tential weakness in our model, we have taken care to ensure that all the results in this study  
157 are not affected by the upper boundary condition, and focus exclusively on the circulation

158 in the stratosphere below the drag layer.

159 Table 1 lists the integrations used in this study. All were integrated for 10,000 days after a  
160 300 day spin up period. Circulation based metrics converged much faster than this, but long  
161 integrations were necessary to quantify the tracer transport. The integrations with  $\gamma = 0$ ,  
162 however, are singular in that there is almost no ventilation of the upper stratosphere above  
163 10 hPa. We avoid analysis of tracer transport in the upper stratosphere in these integrations,  
164 as convergence here is extremely slow. Integrations were run at T42 resolution (triangular  
165 truncation at wavenumber 42), with 40  $\sigma = p/p_s$  (where  $p$  is pressure and  $p_s$  surface pressure)  
166 layers spaced evenly in height  $z$ , as in Polvani and Kushner (2002). Tracers are modeled  
167 in grid space, and advected with a finite-volume parabolic scheme. The robustness of the  
168 model to resolution and numerics has also been investigated, and will be presented in greater  
169 detail in a future paper. We find that the residual mean circulation of the model at T42L40  
170 resolution is very robust to changes in resolution and numerics, as confirmed in simulations  
171 with a finite-volume dynamical core with a cubed sphere grid. Tracer transport, on the other  
172 hand, is sensitive to model numerics and resolution, as found by Eluszkiewicz et al. (2000).  
173 The tracer based results shown in this paper are qualitatively robust, but the quantitative  
174 age of air is sensitive to numerics.

#### 175 *a. Metrics*

176 The “mean age” of stratospheric air and the “age spectrum” quantify the transport times  
177 of tracers through the atmosphere. These measures can be directly related to stratospheric  
178 chemistry processes, as the time air has been in the stratosphere quantifies how long it has  
179 been exposed to ultraviolet radiation and stratospheric reactions (e.g. Waugh and Hall 2002).  
180 Formally, the mean age  $\Gamma(x)$  at a point  $x$  in the atmosphere quantifies the average time it  
181 takes air to get there from the surface, specified as a boundary  $\Omega$ . To compute the age,  
182 one must integrate over all possible pathways from the surface  $\Omega$  to  $x$ , accounting for both  
183 advection and the quasi-horizontal mixing of air parcels along isentropes. Hence in practice

184 we use a tracer to estimate the age, so capturing all the relevant processes. The mean age  
 185 in the stratosphere is on the order of years, compared to on the order of days throughout  
 186 the troposphere, where air is continually in contact with the surface.

187 The age spectrum provides further information on the pathways taken by air from  $\Omega$  to  
 188  $x$ . As established by Hall and Plumb (1994), the age spectrum can be viewed as a Green’s  
 189 Function  $\mathcal{G}(x|\Omega, t)$  which propagates mass (a passive tracer) from the surface  $\Omega$  to  $x$  in time  
 190  $t$ . The mean age is then just the first moment of the age spectrum,

$$191 \quad \Gamma(x) = \int_0^\infty t\mathcal{G}(x|\Omega, t)dt \quad (1)$$

192 Following Waugh and Hall (2002), we quantify the key features of the age spectrum with  
 193 the spectral width  $\Delta$  and the “model age.” The spectral width quantifies the spread of the  
 194 spectrum, that is, the variance of the different paths the tracer takes from the boundary to  
 195  $x$ . It is related to the second momentum of the age spectrum,

$$196 \quad \Delta^2(x) = 1/2 \int_0^\infty (t - \Gamma(x))^2\mathcal{G}(x|\Omega, t)dt. \quad (2)$$

197 The modal age is the mode of the age spectrum, and so tells us the time it takes a tracer to  
 198 reach  $x$  when traveling along the most likely path.

199 We obtain the age spectrum by computing the “Boundary Impulse Response” with a  
 200 pulse tracer (e.g. Hall et al. 1999). Given the stationary forcing of our model, this provides a  
 201 fairly good estimate of the actual age spectrum. We compute the mean age two ways, with  
 202 a “clock tracer” and by taking the mean of the age spectrum, confirming that both yield  
 203 approximately the same mean age. The clock tracer is a conserved tracer whose concentration  
 204 near the surface is forced to linearly increase with time. The mean age is then proportional  
 205 to the difference in concentration of the clock tracer at height and the surface. For both the  
 206 pulse and clock tracer, we define the boundary  $\Omega$  to be the three lowermost  $\sigma$  surfaces, the  
 207 surface layer of the Held and Suarez (1994) forcing. For plotting purposes, we show the age  
 208 relative to the age of air entering the stratosphere at 100 hPa, to minimize any impacts of  
 209 the topography on the tropospheric circulation.

210 The residual mean, or Transformed Eulerian Mean (TEM), circulation approximates the  
 211 Lagrangian transport of mass through the atmosphere (e.g. Edmon et al. 1980; Andrews  
 212 et al. 1987), and can be viewed as an approximation to the zonal-mean circulation in isen-  
 213 tropic coordinates. The residual mean meridional and pressure velocities ( $\overline{v}^*$ ,  $\overline{\omega}^*$ ) and stream  
 214 function  $\psi^*$  are defined by

$$215 \quad \overline{v}^* = \overline{v} - \frac{\partial(\overline{v'\theta'}/\overline{\theta}_p)}{\partial p} = \frac{\partial\psi^*}{\partial p} \quad (3)$$

216 and

$$217 \quad \overline{\omega}^* = \overline{\omega} + \frac{1}{a \cos \phi} \frac{\partial(\cos \phi \overline{v'\theta'}/\overline{\theta}_p)}{\partial \phi} = -\frac{1}{a \cos \phi} \frac{\partial(\psi^* \cos \phi)}{\partial \phi}, \quad (4)$$

218 where an overbar and ' denote the zonal mean and deviations therefrom, and  $v$ ,  $\omega$ ,  $\theta$ , and  $\phi$   
 219 are the meridional wind, pressure velocity, potential temperature, and latitude. As can be  
 220 seen from (3) and (4), the residual mean circulation can be computed directly from the heat  
 221 flux,  $\psi^* = \psi + \overline{v'\theta'}/\overline{\theta}_p$ , where  $\psi$  is Eulerian mean streamfunction. From this perspective, we  
 222 see that residual circulation is given by the Eulerian circulation plus a eddy transport.

### 223 3. Tropospheric versus Stratospheric Control

224 We begin by exploring two controls on the Brewer-Dobson Circulation. The mean age of  
 225 stratospheric air in four integrations of the idealized GCM is shown in Fig. 1. Mass transport  
 226 through the stratosphere is extremely slow in the integrations shown in the top panels, the  
 227 mean age almost 19 years in the upper stratosphere. In the integrations illustrated in the  
 228 lower panels, the air is substantially younger, the oldest air now only 11 years old. The  
 229 “freshening” of the stratosphere between the two integrations on the left was effected by  
 230 introducing surface topography to the model. Both integrations were run with a strong  
 231 polar vortex (equilibrium lapse rate parameter  $\gamma = 4$ ), but in (a) there is no topography,  
 232 while (c) was driven with wave number 2 topography of amplitude  $h_0 = 4$  km. Increased  
 233 wave forcing from the troposphere freshens the stratosphere.

234 The topography, however, is the same in the two integrations on the right. Here the re-

235 duction in mean age was effected by changing the thermal forcing of stratosphere, increasing  
236 the equilibrium lapse rate of the stratospheric polar vortex from  $\gamma = 1.5$  in (b) to  $5 \text{ K km}^{-1}$   
237 in (d). The similarity between the integrations on the left and right suggests that radiative  
238 changes in the stratosphere can have almost the same effect on the mean age as substantial  
239 changes in the wave forcing.

240 Fig. 2 shows the zonal wind climatology of the same four integrations, highlighting the  
241 fact that the influence of topography and stratospheric thermal forcing have very different  
242 impacts on the circulation of the atmosphere, despite the similarity of their influence on  
243 the mean age. Of the two “old” integrations in the upper panels, the simulation without  
244 topography has a much stronger polar vortex. Weaker diabatic forcing, combined with  
245 increased planetary wave driving weakens the polar vortex in the integration in (b) compared  
246 to (a), as discussed by Gerber and Polvani (2009). The climatologies of the two “young”  
247 integrations shown in the lower panels also vary considerably; here however, the strength of  
248 the vortex varies in the opposite sense. Weaker thermal forcing, combined with increased  
249 topography, weakens the jet in the integration shown in (c) relative to that in (d). Fig. 2  
250 suggests that the mean age of stratospheric air can be varied distinctly from the climatology:  
251 there is not a simple one-to-one relationship between vortex strength and mean age.

252 One can begin to understand the impact of the two parameters by comparing the residual  
253 mean circulations, shown in Fig. 3. While the mean age is similar in the two upper and lower  
254 integrations, respectively, the residual circulations are significantly different. Focussing first  
255 on the “old” integrations in the top panels, we see that the total amplitude of the circulation,  
256 measured as the net upwelling at 100 hPa, is substantially larger in the integration in (b),  
257 with weak a vortex and topography, than in the integration in (a) with a strong vortex  
258 but no topography. Near the stratopause, at 1 hPa, however, the circulation of the latter  
259 simulation is stronger. A similar contrast exist between the two “younger” integrations in  
260 the lower panels. While the net residual circulation at 100 hPa is weaker in (d) compared  
261 to (c), the circulation in this integrations extends deeper into the stratosphere. Viewed in

262 terms of the differences between the upper and lower integrations, we find that mean age  
263 can be reduced by increasing (compare a to c) or deepening (b to d) the residual circulation.

264 These four integrations suggest two controls on the Brewer-Dobson Circulation. A first  
265 critical factor is the amplitude of the planetary wave forcing of the stratosphere. We term this  
266 influence tropospheric control, as we will show that the planetary wave forcing is primarily  
267 set by topography and the tropospheric jet structure. The impact of surface topography fits  
268 well with our understanding of the BDC as a mechanically driven circulation (e.g. Haynes  
269 et al. 1991; Holton et al. 1995). A second, perhaps less intuitive control on the Brewer-  
270 Dobson Circulation is the diabatic forcing of the stratosphere itself, here approximate by  
271 changes in the radiative equilibrium profile controlled by  $\gamma$ . Fig. 1 demonstrates that both  
272 factors have a similar impact on mass transport through the stratosphere.

## 273 4. Controls on the Residual Circulation

274 To better understand how tropospheric and stratospheric conditions influence strato-  
275 spheric mass transport, we first systematically explore changes in the residual mean circula-  
276 tion. Fig. 4 shows the residual mean pressure velocity  $\bar{\omega}^*$  at 10 and 100 hPa for two series of  
277 integrations in which the topographic amplitude  $h_0$  and vortex lapse rate parameter  $\gamma$  are  
278 systematically varied. Beginning in the lower stratosphere, panels (c) and (d), we see that  
279 topography has a larger impact on residual circulation into and out of the stratosphere. With  
280 larger topography, upwelling (downwelling) increases uniformly between approximately 30°S  
281 and 20°N (20-90° N). There is little change in the Southern Hemisphere (SH) extratropics,  
282 as the topography is only in the Northern Hemisphere (NH), but the tropical signal is quite  
283 uniform. Clearly planetary wave activity in the NH alone is modulating upwelling through-  
284 out the entire tropical stratosphere. This supports the conclusions of Yulaeva et al. (1994),  
285 who relate colder temperatures in the lower tropical stratosphere in boreal winter relative  
286 to austral winter to greater stationary wave forcing in the NH.

287 At 100 hPa, changes in the thermal forcing have less of a net impact. Inspection of  
 288 the tropics indicates that increasing the strength of the polar vortex reduces the upwelling.  
 289 Increasing  $\gamma$  also shifts the downwelling towards the edge of the polar vortex, increasing it  
 290 near 50°N and weakening it poleward of 60°N. This is consistent with theoretical expectations  
 291 based on Charney and Drazin (1961). Strong winds in the cold vortex limit upward wave  
 292 propagation, so reducing the net wave driving. However, this is partially compensated by  
 293 increased wave driving and downwelling on the edge of the vortex, so there is less of a  
 294 decrease in the mechanical driven transport than one might expect.

295 At 10 hPa, the impact of topography on  $\bar{\omega}^*$  is about the same as at 100 hPa; increased  
 296 planetary wave forcing increases vertical motion, although there is some saturation for large  
 297 values of  $h_0$ . The impact of vortex strength, however, is qualitatively different. The vertical  
 298 motion at this level scales almost linearly with  $\gamma$ : increasing the strength of the vortex  
 299 increases the residual circulation. This confirms the deepening of the circulation suggested  
 300 in Fig. 3b and d.

301 We relate changes in the residual circulation to changes in the resolved wave forcing  
 302 in Fig. 5. Panels (a) and (b) capture the essential impacts of topography and  $\gamma$  on the  
 303 residual mean circulation, showing the net downwelling in each hemisphere as a function of  
 304 height. By downward control, the net residual circulation across at a given pressure level is  
 305 a function of the wave forcing above it (Haynes et al. 1991). We confirm this relationship  
 306 in the model integrations in Fig. 5c and d, which illustrate the total wave driving in each  
 307 integration. Specifically, for each hemisphere we plot

$$308 \quad \tau(p) = \frac{2\pi r_0^2}{g} \int_{\text{pole}}^{\text{equator}} f \frac{\overline{v'T'}}{\theta_p} \cos^2 \phi d\phi, \quad (5)$$

309 the net Eliassen-Palm (E-P) flux of wave activity across a pressure surface  $p$ . As any net wave  
 310 activity that propagates across a given pressure level must break above it, this measure is  
 311 related to the net torque on the atmosphere above each pressure level. The torque is negative,  
 312 or easterly, in both hemispheres, but we reverse the sign in the NH for clarity.

313 In Fig. 5a, we see that increasing the topography uniformly increases the residual circu-

314 lation throughout the stratosphere, though changes appear to saturate in the upper strato-  
315 sphere for increasingly large topography. This follows the increase in wave driving throughout  
316 the stratosphere shown in (c). Increasing the vortex strength, however, primarily affects the  
317 depth of the upwelling, as seen in Fig. 5b. At 80 hPa, there is almost no effect on the  
318 upwelling; below this point, a colder vortex reduces the circulation, but above, it increases  
319 it. This can be related to the redistribution of wave breaking illustrated in (d). Increasing  
320  $\gamma$  allows waves to propagate higher into the stratosphere, increasing wave breaking at upper  
321 levels, which in turn deepens the residual circulation.

322 The relationship between the residual circulation and the wave forcing is not perfect  
323 in Fig. 5 because we have neglected the horizontal structure of the wave driving. Due to  
324 the weakening of the Coriolis force at lower latitudes, the same torque can effect a larger  
325 circulation if it is shifted equatorward. Hence the meridional transport of momentum by  
326 eddy fluxes also affects the transport. Downward control calculations (not shown) confirm  
327 that the differences in upwelling can be fully explained by changes in wave driving. These  
328 calculations also allow us to ensure that our results are not skewed by the Rayleigh friction  
329 near the model top. We find that changes in the sponge layer, in response to changes in the  
330 wind structure, have little effect on the transport. The impact is minimal in simulation with  
331 varying topography. Increasing  $\gamma$  does increase the circulation driven by the sponge layer,  
332 but the changes are a factor of 10 or more smaller than those driven by changes in resolved  
333 wave driving at 10 hPa, and matter even less lower in the stratosphere.

#### 334 *a. Tropospheric Control*

335 The impact of increased surface topography on the BDC on the model is very much in  
336 keeping with our current understanding of the stratospheric circulation (e.g. Holton et al.  
337 1995). One would expect larger topography to excite larger stationary waves, so increasing  
338 the wave forcing and driving a stronger residual circulation. This initial impression is correct,  
339 provided one is careful to specify *where* there stationary waves are larger. As shown in Fig. 6a,

340 increasing the topographic forcing increases the amplitude of the stationary wave at the base  
341 of the stratosphere. In the stratosphere itself, however, the wave amplitude does not scale  
342 with the topography: initially it increases with  $h_0$ , reaching a maximum for  $h_0=2$  km, and  
343 then drops down again, so that above 10 hPa, the wavenumber 2 amplitude is smaller for  
344  $h_0=4$  than for  $h_0=1$  km. The increased circulation and wave forcing observed in Fig. 5a and  
345 c is well correlated with the stationary wave amplitude in the upper troposphere and lower  
346 stratosphere, but not with the wave amplitude within the stratosphere.

347 The surface topography controls the amplitude of the standing waves in the troposphere,  
348 but in the stratosphere, vortex conditions also play a role in the wave amplitude, as can be  
349 seen in Fig. 6b, where the surface topography is fixed at  $h_0=3$  km and  $\gamma$  is systematically  
350 varied. For fixed topography, a colder vortex creates a resonant cavity in the stratosphere  
351 leading to stronger stationary waves (e.g. Matsuno 1970). When the vortex forcing is kept  
352 constant, however, the the stationary waves generated by topography have a nonlinear impact  
353 on the vortex. As documented by Gerber and Polvani (2009), topography reduces the  
354 amplitude of the vortex, having a similar effect as  $\gamma$  on the mean state.

355 To understand the wave amplitude, one must account for wave propagation and reflection  
356 (e.g. Harnik and Lindzen 2001). In Fig. 7, we show the stationary waves for the integrations  
357 with  $h_0 = 1$  and 4 km. For the latter integration, the stationary wave exhibit a strong  
358 westward tilt with height, implying vertical propagation. This leads to strong wave breaking  
359 throughout the stratosphere, reducing the strength of the polar vortex. For the integration  
360 with weak topography, the wave amplitude increases considerably with height, reaching a  
361 maximum near 3 hPa, but the westward phase tilt is substantially diminished. The polar  
362 vortex in this simulation is much stronger (differences between these integrations are similar  
363 to those shown in Fig. 2a and c), forming a resonant cavity. Thus, the wave amplitude in this  
364 integration is quite large in the stratosphere, but less wave activity is actually propagating  
365 upward.

366 We also explore the impact of different topographic structure. Wavenumber 1 has a

367 similar impact as wavenumber 2, but the transmission of the wave from the surface to the  
368 upper troposphere / lower stratosphere is not as linear as with wavenumber 2 topography.  
369 As seen in Fig. 7c, for topography up to amplitude  $h_0=3$  km, the stationary wave at the  
370 base of the stratosphere changes little, and only begins to increase substantially for larger  
371 values of  $h_0$ . As with wavenumber 2 topography, however, the wave forcing throughout the  
372 stratosphere scales with the wave amplitude in the upper troposphere / lower stratosphere,  
373 as seen in Fig. 8a. Consistent with the theoretical analysis of Charney and Drazin (1961),  
374 higher wavenumber topography is inefficient at driving the stratospheric circulation. This is  
375 confirmed in Fig. 8b, where we illustrate the impact of the topographic wavenumber on the  
376 wave driving.

#### 377 *b. Stratospheric Control*

378 Understanding the impact of  $\gamma$  on the BDC is perhaps less intuitive. Absent any mechan-  
379 ical forcing, the stratosphere would simply relax to radiative equilibrium, and there would  
380 be no residual mean circulation (e.g. Andrews et al. 1987, p.300-302). Hence the change in  
381 the circulation effected by  $\gamma$  must be indirect, by modifying the behavior of the waves.

382 Charney and Drazin (1961) showed that while westerly winds are necessary for the prop-  
383 agation of a Rossby wave, if the winds become too strong, the wave cannot maintain itself  
384 against downstream advection. The intrinsic easterly phase speed of a wave decreases with  
385 spatial scale (increased wavenumber), so as the winds increase, shorter wavelengths can no  
386 longer propagate vertically. Charney and Drazin (1961) found that stratospheric wind ve-  
387 locities in the winter are so great that synoptic waves are inhibited, and only the gravest  
388 planetary winds have a chance of propagating in the vertical. Neglecting the horizontal  
389 structure of the winds, then, one would expect a colder vortex to suppress wave propaga-  
390 tion. Absent topography, this intuition is correct. As shown in Fig. 8c, and analyzed by  
391 Kushner and Polvani (2004), wave activity decreases with increased  $\gamma$  in this case.

392 In the presence of topography, however, Fig. 5 suggests that the vortex's influence on

393 wave activity depends where you look in altitude. Wave activity at 100 hPa is decreased  
 394 when the vortex is cooled, but above 70 hPa, increasing  $\gamma$  allows more wave activity to  
 395 propagate upward. The key lies in the meridional structure of the flow;  $\gamma$  induces a cooling  
 396 of the polar vortex relative to the midlatitude and tropical stratosphere. Even for a very  
 397 strong vortex, however, there is always a region where wave propagation is possible.

398 The refractive index  $n^2$  was introduced by Matsuno (1970) to account for the two dimen-  
 399 sional structure of the polar vortex. He derived a two-dimensional wave equation in the form  
 400  $\xi_{zz} + \xi_{yy} + n^2\xi = 0$  for a wave quantity  $\xi$ . Wavelike solutions are possible when  $n^2$  is positive,  
 401 while only evanescent solutions exists when  $n^2$  is negative. Following the formulation by  
 402 Harnik and Lindzen (2001), we define  $n^2$  by

$$403 \quad n^2 = \left[ \frac{\bar{q}_\phi}{r_0(\bar{u} - c)} - \left( \frac{k}{r_0 \cos \phi} \right)^2 - \frac{F(N^2)}{f^2} \right], \quad (6)$$

404 where  $\bar{q}_\phi/r_0$  is the meridional gradient in potential vorticity,

$$405 \quad \frac{\bar{q}_\phi}{r_0} = \bar{q}_y = \beta - \frac{1}{r_0^2} \left[ \frac{(\bar{u} \cos \phi)_\phi}{\cos \phi} \right]_\phi + \frac{f^2}{R_d} \left( \frac{p\bar{\theta} \bar{u}_p}{T \bar{\theta}_p} \right)_p. \quad (7)$$

406 The notation is standard, with  $r_0$  the radius of the earth,  $u$  the zonal wind,  $c$  and  $k$  the  
 407 phase speed and zonal wavenumber of the wave,  $\phi$  the latitude in radians,  $f = 2\Omega \sin \phi$  and  
 408  $\beta$  the Coriolis parameter and its meridional derivative, respectively,  $R_d$  the gas constant of  
 409 dry air,  $p$  pressure, and  $\theta$  and  $T$  the potential and standard temperatures. If  $N$  is constant,  
 410 the function  $F(N^2)$ , detailed in Harnik and Lindzen (2001), reduces to  $1/(NH)^2$ , where  $H$  is  
 411 the scale height. While  $N$  is not constant in our model, we follow Simpson et al. (2009) and  
 412 make this approximation, as  $F(N^2)$  involves high order derivatives of temperature, leading  
 413 to concerns about numerical inaccuracy. All results, however, are qualitatively the same if  
 414 the full  $F(N^2)$  is used.

415 Fig. 9 illustrates the relationship between wave driving, as quantified by the divergence of  
 416 the Eliassen-Palm flux (Edmon et al. 1980), and the index of refraction for stationary waves  
 417 ( $c = 0$ ) of wavenumber  $k = 2$  (the dominant wave forced by our surface topography) for three  
 418 integrations with varying vortex cooling parameter  $\gamma$ . On the left, we show the key elements

419 that cause changes in  $n^2$ , the meridional potential vorticity gradient  $\bar{q}_y$  and zonal mean zonal  
420 wind  $\bar{u}$ . In the case of no polar vortex,  $\gamma = 0$  shown in Fig. 9a and b, the reduction in wave  
421 driving in the mid to upper stratosphere can readily be understood in terms of the zero wind  
422 line across the lower stratosphere. Most waves break in the neighborhood of the critical line,  
423 and the residual mean circulation is very shallow.

424 For a strong vortex,  $\gamma = 6$ , the net reduction of wave activity in the lower stratosphere is  
425 related to the throttle on the wave propagation at the base of the stratosphere, the region of  
426 negative  $n^2$  at 40 N and 100 hPa in Fig. 9f. Waves that get past this point through tunneling  
427 and changes in the index with time, however, experience a broader wave guide in the mid  
428 stratosphere relative to the simulations with weak  $\gamma$  (Fig. 9d), particularly in the region of  
429 10-50 hPa. The key difference is the downward extension of potential vorticity gradients with  
430 the strengthening vortex and the increasing width of westerly flow, as seen by comparing  
431 Fig. 9c and e. The strong vortex creates a waveguide deeper into the stratosphere, allowing  
432 waves to propagate to higher altitudes.

433 While the index of refraction provides a qualitative explanation for the behavior of the  
434 model, we stress that it is important not to over interpret results based on linear theory and  
435 the mean state. As shown in Fig. 2, the mean state itself is a function of both the wave  
436 driving and stratospheric thermal forcing. A given mean state does not uniquely describe  
437 the wave forcing, that is, a colder vortex can be obtained by cooling the stratosphere or  
438 reducing the stationary wave forcing from the troposphere. The index of refraction is based  
439 only on the mean state, and so varies similarly when  $\gamma$  is fixed and the topography is varied  
440 (not shown). When the topography is changed, however, the index implies a false sense  
441 of causality. The vortex is weaker in cases of larger topography, which would suggest that  
442 there is less room for waves to propagate, but in this case the waveguide is weaker precisely  
443 because there is more wave breaking. The qualitative analysis based on the index of refraction  
444 alone only works if the wave driving at the base of the stratosphere is held fixed, as in the  
445 integrations shown in Fig. 9.

## 5. Relationship between the residual mean circulation and mass transport

Fig. 5 shows that the changes in the the residual circulation are driven by changes in wave driving in the winter (NH) hemisphere. To understand how these changes affect mass transport, and so the differences in mean age observed in Fig. 1, we must connect the residual circulation to tracer transport.

The upper panels of Fig. 10 show the mean age of air at the equator at three pressure levels as a function of topographic height  $h_0$  and lapse rate parameter  $\gamma$ . The decrease in age with topography is fairly linear with  $h_0$  at all levels, with some saturation at larger amplitudes. The relationship is more complicated for  $\gamma$ . The age is very sensitive for small values, particularly at upper levels, and then saturates at larger amplitudes. The integration with  $\gamma = 0$ , in fact, is singular in the upper stratosphere, as the residual circulation vanishes above 10 hPa. Hence the age at 1 hPa was not nearly converged after almost three decades of integration. The lower panels of Fig. 10 show net tropical upwelling as a function of  $h_0$  and  $\gamma$ . As one would expect based on an advection-diffusion model (e.g. Waugh and Hall 2002), changes in upwelling tend to be the mirror image of changes in age. For the case of varying topography, younger air is associated with greater upwelling. The situation is more complicated for changes in upwelling driven by  $\gamma$ , shown in Fig. 10d. The trends in upwelling mirror changes in age at upper levels (35 and 10 hPa), but at 100 hPa, the tropical upwelling *decreases* at the same time as the age in the stratosphere above *decreases*.

Clearly, the net transport into the stratosphere (or across a particular pressure surface), may not be easily connected to the age. To highlight the relationship between age and the residual circulation, we show scatter plots of the residual velocity  $\bar{\omega}^*$  and the mean age in Fig. 11. Both panels show the relationship between the upwelling at the equator, which is a good proxy for the total tropical transport, with the age at the equator and 10 hPa. On the left, the plot is based on  $\bar{\omega}^*$  at 100 hPa: as suggested by Fig. 10, there is significant

472 scatter. Transport into the stratosphere is not correlated with the age across all of the  
 473 integrations, with an correlation coefficient near zero. A linear relationship is found if one  
 474 focusses only on changes associated with topography, the blue squares, but the relationship  
 475 is the opposite when  $\gamma$  is varied, the red circles. Focussing on the upwelling at 28 hPa,  
 476 however, as shown in the right panel, one find a fairly linear relationship between age and  
 477 upwelling across all the simulations, with a correlation coefficient  $R = 0.98$ . The slope of  
 478 the scatter, approximately  $1.5 \text{ yr}/(\text{Pa day}^{-1})$ , quantifies the sensitivity of the age to changes  
 479 in upwelling: a  $1 \text{ Pa day}^{-1}$  reduction in upwelling at 28 hPa leads to a 1.5 year increase in  
 480 mean age at 10 hPa. We note, however, that the age is quantitatively sensitive to model  
 481 numerics, and so will focus on the qualitative link between age and upwelling reflected in  
 482 the correlation coefficient.

483 The relationship between the residual circulation and the mean age at a given point  
 484 depends on the structure of the residual circulation. This structure can be characterized by  
 485 repeating the analysis shown in Fig. 11 at all points in latitude-pressure space, retaining the  
 486 correlation coefficient  $R$  as measure of the coherence. Fig. 12 shows the correlation between  
 487  $\bar{\omega}^*$  and  $\bar{v}^*$  and the age at the equator and 10 hPa. Panel (a) shows that the age at this  
 488 point in the atmosphere is strongly correlated with upwelling across the tropics just below  
 489 it, and, by conservation of mass, downwelling in the extratropics of the winter hemisphere.  
 490 The positive correlation deep into the Southern Hemisphere is due to the fact that there is  
 491 no seasonal cycle. Changes in the upwelling in the tropics are correlated with upwelling deep  
 492 into the summer hemisphere, although the amplitude here is extremely small.

493 The correlation with the residual meridional velocity  $\bar{v}^*$  shown in Fig. 12b is, in contrast,  
 494 stronger above the target point (10 hPa and the equator). This stems from the conservation  
 495 of mass: any mass brought up from below this point must be advected away above it. Hence a  
 496 larger meridional velocity above implies more upwelling and so younger air. The meridional  
 497 velocity also highlights the connection to the summer hemisphere. Age at the equator is  
 498 strongly anti-correlated with northward transport of air across the tropics toward the winter

499 pole.

500 Thus far we have focussed primarily on the mean age. As shown in the first two columns  
501 of Fig. 13, the properties of the age spectrum largely follow the mean age. In the first  
502 column, we show the spectral width  $\Delta$  for the four key integrations shown in Figs. 1-3. The  
503 width is substantial larger in the two “old” integrations, where there is no topography or  
504 the vortex is very weak. The spectral width is largest in the lower stratosphere, particularly  
505 for the integration with  $\gamma=4$  and  $h_0=0$  (panel a), suggesting a wide variance in how parcels  
506 reach this region, faster through mixing from the troposphere, or slower along trajectories  
507 through the deep circulation high into the stratosphere. The spectral width is slightly  
508 smaller in the other old integration, with  $\gamma=1.5$  and  $h_0=3000$  (panel d). The modal age in  
509 this integration, however, is slightly larger, as shown in the second column of Fig. 13. The  
510 modal age quantifies the time it takes a tracer to reach a given point in the atmosphere along  
511 the most likely pathway. In this integration, parcels are more slowly advected up into the  
512 upper stratosphere, but there is less variance in the trajectories. The two effects cancel each  
513 other out, so that the two “old” integrations have about the same mean age in the upper  
514 stratosphere.

515 The model age highlights the potential isolation of air over the pole by the stratospheric  
516 polar vortex. The modal age is higher in the lower polar stratosphere (c. 50 hPa) in the  
517 integrations shown in Fig. 13b and k, despite the fact that their mean age is quite different.  
518 As shown in Fig. 2, the unifying element in these two integrations is the strength of the  
519 polar vortex. A strong polar night jet leads to enhanced potential vorticity gradients on the  
520 vortex edge, which in turn inhibits mixing along isentropic surfaces (e.g. Bühler and Haynes  
521 1999; Sobel and Plumb 1999). In these integrations, then, mass transport is dominated by  
522 the slow, deep circulation from above.

523 The impact of the vortex on mixing along isentropes is more clearly visible in the merid-  
524 ional gradient in the mean age, shown in third column of Fig. 13. Gradients in the mean  
525 age reveal transport barriers in the stratosphere. In all integrations, there is evidence of the

526 two main barriers to transport, separated by a well mixed “surf zone” between roughly 30  
527 and 60 degrees (e.g. McIntyre and Palmer 1983; Plumb 2002). The tropical barrier, centered  
528 near 20 degrees, is the most prominent, but a secondary barrier on the edge of the polar  
529 vortex is visible at 70 degrees in all integrations. The strength of the transport barriers in  
530 the winter hemisphere, however, are not well correlated with the mean age. The barriers are  
531 stronger in the “old” integration with  $\gamma=0$  and  $h_0=0$  (Fig. 13c) and the “young” integration  
532 with  $\gamma=5$  and  $h_0=3000$  (Fig. 13l). As with the model age discussed above, the key unifying  
533 factor in these integrations is the strength of the polar vortex. As seen in Fig. 9, potential  
534 vorticity gradients are increased on both sides of the surf zone when the vortex is stronger,  
535 inhibiting mixing.

536 In summary, the age of air in the mid to upper stratosphere depends critically on the  
537 ability of the residual circulation to bring mass up from the lower stratosphere. It is thus  
538 controlled by the “deep” branch of the residual mean circulation, and so equally sensitive to  
539 changes in wave forcing and the diabatic forcing of the stratosphere. Mixing along isentropic  
540 surfaces, important for ventilating the lower polar stratosphere, however, is more sensitive  
541 to the strength of potential vorticity gradients established by the polar vortex.

## 542 **6. Impacts on the Tropopause and Cold Point**

543 By focussing on the age of the air, we have emphasized the impact of the stratospheric  
544 circulation on the mass transport, which is most directly relevant to stratospheric ozone  
545 chemistry. The Brewer-Dobson Circulation can also impact tropospheric climate by shaping  
546 the tropopause (Birner 2010) and altering the water vapor content of the stratosphere by  
547 modulating the temperature of the tropical cold point (Mote et al. 1996).

548 Fig. 14 quantifies changes in the tropopause height, as defined with the conventional  
549 World Meteorological Organization (WMO) criteria, the level at which the lapse rate drops  
550 below  $-2 \text{ K km}^{-1}$ . Panels (a) and (b) show that increased topography raises the tropopause in

551 the tropics, particularly at its borders, near 30°N and S. By increasing the residual circulation  
552 in the lower stratosphere, topography cools the atmosphere in the tropics and warms it in the  
553 extratropics. As suggested by the radiative constraint on tropopause height in Held (1982),  
554 a cooling (warming) of the lower stratosphere will lift (lower) the tropopause (see also Vallis  
555 2006, Chpt. 12). We also emphasize the uniform response of the tropics, despite the fact that  
556 topography forcing is only in the winter hemisphere. The model suggests that the equator  
557 to pole gradient in the tropopause can be increased by nearly 2 km by increasing the BDC  
558 in the lower stratosphere. This supports the conclusions of Birner (2010), who found that  
559 the stratospheric circulation plays an important role in the contrast in the tropopause height  
560 between the tropics and high latitudes.

561 Changes in  $\gamma$ , shown in 14c and d, have a smaller effect on the tropical tropopause. When  
562  $\gamma$  is decreased, there is a small rise in the tropical tropopause due to increased upwelling.  
563 There are more significant impacts in the extratropics, where warming of the vortex lowers  
564 the tropopause at the pole by over a kilometer. This is driven by local changes in down-  
565 welling, as seen in Fig. 4d, where increased  $\gamma$  pushes the region of maximum downwelling  
566 equatorward. A colder vortex refracts planetary wave activity away from the pole, reducing  
567 the downwelling in the high latitudes.

568 Fig. 15 illustrates changes in the cold point temperature and pressure induced by varying  
569 topographic and stratospheric vortex forcing. The results are closely related to changes in  
570 the tropical tropopause height. Fig. 15a shows that increased upwelling driven by changes in  
571 planetary waves can cool the cold point approximately a degree and half, raising it 20 hPa  
572 higher in the atmosphere. Changes in response to  $\gamma$  are more subtle, on the order of half a  
573 degree. This response is driven by the slight weakening of the tropical upwelling in response  
574 to a colder vortex.

575 These results suggest that tropospheric control on planetary wave forcing plays the largest  
576 role in the impact of the Brewer-Dobson Circulation on the tropopause and cold point.  
577 These metrics are most sensitive to “shallow branch” of the BDC, and so less dependent on

578 conditions in the polar vortex above. This said, we stress that the impact of topography is not  
579 necessarily local. Changes in planetary wave forcing in the extratropical winter hemisphere  
580 alone have a significant impact across the entire tropics, deep into the summer hemisphere.

## 581 **7. Conclusions**

582 We have explored factors that control the strength and structure of the Brewer-Dobson  
583 Circulation in an idealized General Circulation Model, linking changes in the residual mean  
584 circulation to changes in mass transport. We have shown that the diabatic forcing of the  
585 stratosphere and planetary wave forcing by the troposphere can have comparable effects on  
586 the mean age of air in the mid to upper stratosphere. Their impact on the age, however,  
587 is mediated through different controls on the residual circulation. Increased planetary wave  
588 forcing leads to an overall increase in the strength of the BDC, particularly the lower branch  
589 of the circulation, an effect we term tropospheric control. A colder polar vortex, on the  
590 other hand, creates a waveguide higher into the stratosphere, raising the breaking level of  
591 the planetary waves and deepening the circulation, an effect we term stratospheric control.  
592 Ventilation of mass in the mid to upper stratosphere depends critically on penetration of  
593 tropical upwelling deep into the stratosphere, and so the age of air is comparably sensitive  
594 to both tropospheric and stratospheric controls.

595 Planetary wave activity was modified by altering surface orography. Following Gerber  
596 and Polvani (2009), we explored changes in the amplitude and wavenumber of idealized  
597 topography in the model's winter hemisphere. We found that wave breaking through the  
598 depth of the stratosphere is well correlated with the amplitude of stationary, planetary scale  
599 waves 1 and 2 at the base of the stratosphere. The relationship between wave breaking and  
600 the amplitude of the mountains at the surface is not as tight, as tropospheric dynamics do  
601 not always linearly transmit the surface signal to the stratosphere. The relationship between  
602 wave amplitude in the stratosphere and wave driving, however, is highly nonlinear. In the

603 stratosphere, stationary wave amplitude depends more critically on the strength of the polar  
604 vortex, as a strong polar vortex sets up a resonant cavity and increases wave reflection.  
605 Reflection can lead to large stationary waves with little vertical phase tilt, and consequently  
606 little propagation of wave activity.

607 The thermal structure of the stratosphere was altered by varying the parameter  $\gamma$  of the  
608 Polvani and Kushner (2002) model, the lapse rate of the equilibrium temperature profile in  
609 the winter hemisphere. A colder equilibrium profile leads to a stronger polar night jet. The  
610 diabatic forcing cannot directly force the Brewer-Dobson Circulation, and so can only affect  
611 it indirectly by modifying the wave breaking. The theoretical work of Charney and Drazin  
612 (1961) would suggest that a stronger vortex will limit Rossby wave propagation into the  
613 stratosphere, thus reducing the amplitude of the Brewer-Dobson Circulation. In the lower  
614 stratosphere, this intuition is correct, as the net wave forcing of the stratosphere is reduced  
615 when the vortex is colder, especially when there is no stationary wave forcing in the lower  
616 stratosphere, as explored by Kushner and Polvani (2004). At upper levels, however, wave  
617 breaking *increases* with a colder vortex, as potential vorticity gradients along the edge of  
618 the vortex create a waveguide higher into the stratosphere.

619 The mean age of air in the mid and upper stratosphere depends on the deep Brewer-  
620 Dobson Circulation, the upwelling of air high into the stratosphere. It is therefore sensitive  
621 to both changes in planetary waves forcing from the troposphere and the diabatic forcing of  
622 the stratosphere. Younger air is associated with a narrower spectral width, which signifies  
623 less variance in the tracer trajectories, and a reduced modal age, suggesting more direct  
624 transport. Mass transport into the lower polar stratosphere, however, is also sensitive to  
625 the strength of polar vortex, as strong potential vorticity gradients inhibit mixing along  
626 isentropes, isolating the polar air.

627 The tropopause and tropical cold point, on the other hand, depend primarily on the  
628 shallow Brewer-Dobson Circulation, the upwelling in the lower stratosphere, and thus are  
629 most sensitive to changes in planetary wave forcing from the troposphere. An increase in

630 the BDC driven by extratropical planetary wave forcing can increase the equator-to-pole  
631 gradient of the tropopause by 2 km and cool the cold point by 1.5 degrees. Changes in  
632 stratospheric polar vortex exclusively above 100 hPa, however, still have a measurable effect  
633 on the tropical cold point and the tropopause, particularly in the extratropics.

634 In using an idealized GCM, we have neglected the important impact of small scale grav-  
635 ity waves on the Brewer-Dobson Circulation. Preliminary work with orographic and non-  
636 orographic gravity wave parameterizations in the model, however, indicates that our main  
637 conclusions are robust. Changes induced by parameterization of orographic waves are in fact  
638 largely compensated by equal and opposite changes in the resolved waves, leaving less impact  
639 on the BDC than might be expected. The impact of non-orographic gravity wave drag is  
640 leading order in the mesosphere, but not in the stratospheric region where we have focussed  
641 in this study. We have investigated the impact of model resolution and numerics on our con-  
642 clusions. We find that the structure of the residual mean circulation is very robust to changes  
643 in resolution and numerics, but that the quantitative properties of tracer transport is not,  
644 consistent with analysis of a more comprehensive Chemistry-Climate Model by Eluszkiewicz  
645 et al. (2000). Hence we have focused on qualitative changes in the tracer transport in this  
646 paper. Results on the robustness to both numerics and gravity wave parameterization will  
647 be documented in future publications.

648 As discussed in the introduction, the increasing trend in the BDC in comprehensive cli-  
649 mate models appears to be at odds with the best available observations. A recent study by  
650 Bönisch et al. (2011), however, sought to reconcile the seemingly disparate trends by consid-  
651 ering changes in the structure of the overturning. Specifically, they suggest that an increase  
652 in the overturning in the lower stratosphere could explain model results, while a slowing in  
653 the deep overturning could increase the mean age in the mid to upper stratosphere. Our  
654 results suggest such circulation trends are possible, if the changes are driven by trends in  
655 both the planetary wave forcing and radiative conditions in the stratosphere. As illustrated  
656 in Fig. 16, by reducing  $\gamma$  while increasing  $h_0$ , the residual mean circulation in the lower

657 stratosphere increases simultaneously with the mean age in the mid and upper stratosphere,  
658 due to a strengthening and shallowing of the residual circulation. We strongly emphasize,  
659 however that this result only suggests that *possibility* that these paradoxical trends could  
660 be reconciled by such circulation trends. Garcia et al. (2011) show that sampling limita-  
661 tions in observations leads to significant uncertainty, and it is quite possible that the the  
662 apparent contradiction between models and observations is due to limitations on available  
663 measurements.

664 *Acknowledgments.*

665 This research was in part supported by a grant from the National Science Foundation to  
666 New York University (NYU). I thank the NYU High Performance Computing center, where  
667 the integrations were performed, and the Max Planck Institute of Meteorology in Hamburg,  
668 Germany, which hosted me while much of this study was finalized.

## REFERENCES

- 671 Andrews, D. G., J. R. Holton, and C. B. Leovy, 1987: *Middle Atmosphere Dynamics*. Aca-  
672 demic Press, Inc., 489 pp.
- 673 Arblaster, J. M. and G. A. Meehl, 2006: Contributions of external forcings to Southern  
674 Annular Mode trends. *J. Climate*, **19**, 2046–2062.
- 675 Birner, T., 2010: Residual circulation and the tropopause structure. *J. Atmos. Sci.*, **67**,  
676 2582–2600.
- 677 Bönisch, H., A. Engel, T. Birner, P. Hoor, D. W. Tarasick, and E. A. Ray, 2011: On the  
678 structural change in the Brewer-Dobson circulation after 2000. *Atmos. Chem. Phys.*, **11**,  
679 3937–3948.
- 680 Brewer, A. W., 1949: Evidence for a world circulation provided by the measurements of  
681 helium and water vapour distribution in the stratosphere. *Quart. J. Roy. Meteor. Soc.*,  
682 **75**, 351–363.
- 683 Bühler, O. and P. H. Haynes, 1999: Constraints on the mean mass transport across potential  
684 vorticity contours. *J. Atmos. Sci.*, **56**, 942–947.
- 685 Butchart, N. and A. A. Scaife, 2001: Removal of chlorofluorocarbons by increased mass  
686 exchange between the stratosphere and troposphere in a changing climate. *Nature*, **410**,  
687 799–802.
- 688 Charney, J. G. and P. G. Drazin, 1961: Propagation of planetary-scale disturbances from  
689 the lower into the upper atmosphere. *J. Geophys. Res.*, **66**, 83–109.
- 690 Dobson, G. M. B., 1956: Origin and distribution of polyatomic molecules in the atmosphere.  
691 *Proc. R. Soc. London Ser. A*, **236**, 187–193.

692 Dobson, G. M. B., D. N. Harrison, and J. Lawrence, 1929: Measurements of the amount of  
693 ozone in the earth's atmosphere and its relation to other geophysical conditions. Part III.  
694 *Proc. R. Soc. London Ser. A*, **122**, 456–486.

695 Dunkerton, T. J., 1989: Nonlinear Hadley circulation driven by asymmetric differential  
696 heating. *J. Atmos. Sci.*, **46**, 956–974.

697 Edmon, H. J., B. J. Hoskins, and M. E. McIntyre, 1980: Eliassen-Palm cross sections for  
698 the troposphere. *J. Atmos. Sci.*, **37**, 2600–2616.

699 Eluszkiewicz, J., R. S. Hemler, J. D. Mahlman, L. Bruhwiler, and L. L. Takacs, 2000:  
700 Sensitivity of age-of-air calculations to the choice of advection scheme. *J. Atmos. Sci.*, **57**,  
701 3185–3201.

702 Engel, A., et al., 2009: Thirty years of stratospheric mean age tracer measurements: no  
703 observable change in the stratospheric circulation. *Nature Geoscience*, **2**, 28–31.

704 Eyring, V., T. G. Shepherd, and D. W. Waugh (Eds.), 2010: *SPARC Report on Chem-*  
705 *istry Climate Model Validation*. SPARC Report No. 5, WCRP-X, WMO/TD-No. X.  
706 <http://www.atmosp.physics.utoronto.ca/SPARC>.

707 Garcia, R. R. and W. J. Randel, 2008: Acceleration of the Brewer-Dobson circulation due  
708 to increases in greenhouse gases. *J. Atmos. Sci.*, **65**, 2731–2739.

709 Garcia, R. R., W. J. Randel, and D. E. Kinnison, 2011: On the determination of the age of  
710 air trends from atmospheric trace species. *J. Atmos. Sci.*, **68**, 139–145.

711 Gerber, E. P. and L. M. Polvani, 2009: Stratosphere-troposphere coupling in a relatively  
712 simple AGCM: The importance of stratospheric variability. *J. Climate*, **22**, 1920–1933.

713 Hall, T. M. and R. A. Plumb, 1994: Age as a diagnostic of stratospheric transport. *J.*  
714 *Geophys. Res.*, **99**, 1059–1070.

715 Hall, T. M., D. W. Waugh, K. A. Boering, and R. A. Plumb, 1999: Evaluation of transport  
716 in stratospheric models. *J. Geophys. Res.*, **104**, 18 815–11 839.

717 Harnik, N. and R. S. Lindzen, 2001: The effect of reflecting surfaces on the vertical structure  
718 and variability of stratospheric planetary waves. *J. Atmos. Sci.*, **58**, 2872–2894.

719 Haynes, P. H., C. J. Marks, M. E. McIntyre, T. G. Shepherd, and K. P. Shine, 1991: On  
720 the "downward control" of extratropical diabatic circulations by eddy-induced mean zonal  
721 forces. *J. Atmos. Sci.*, **48**, 651–678.

722 Held, I. M., 1982: On the height of the tropopause and the static stability of the troposphere.  
723 *J. Atmos. Sci.*, **39**, 412–417.

724 Held, I. M. and M. J. Suarez, 1994: A proposal for the intercomparison of the dynamical  
725 cores of Atmospheric General Circulation Models. *Bull. Am. Meteor. Soc.*, **75**, 1825–1830.

726 Holton, J. R., P. H. Haynes, M. E. McIntyre, A. R. Douglass, R. B. Rood, and L. Pfister,  
727 1995: Stratosphere-troposphere exchange. *Rev. Geophys.*, **33**, 403–439.

728 Kushner, P. J. and L. M. Polvani, 2004: Stratosphere-troposphere coupling in a relatively  
729 simple AGCM: The role of eddies. *J. Climate*, **17**, 629–639.

730 Li, F., J. Austin, and J. Wilson, 2008: The strength of the Brewer-Dobson circulation in a  
731 changing climate: coupled chemistry-climate model simulations. *J. Climate*, **21**, 40–57.

732 Matsuno, T., 1970: Vertical propagation of stationary planetary waves in the winter Northern  
733 Hemisphere. *J. Atmos. Sci.*, **27**, 871–883.

734 McIntyre, M. E. and T. N. Palmer, 1983: Breaking planetary waves in the stratosphere.  
735 *Nature*, **305**, 593–600.

736 McLandress, C. and T. G. Shepherd, 2009: Impact of climate change on stratospheric sudden  
737 warmings as simulated by the Canadian Middle Atmosphere Model. *J. Climate*, **22**, 5449–  
738 5463, doi: 10.1175/2009JCLI3069.1.

739 McLandress, C., T. G. Shepherd, J. F. Scinocca, D. A. Plummer, M. Sigmond, A. I. Jonsson,  
740 and M. C. Reader, 2011: Separating the dynamical effects of climate change and ozone  
741 depletion. Part II: Southern hemisphere troposphere. *J. Climate*, **24**, 1850–1868.

742 Mote, P. W., et al., 1996: An atmospheric tape recorder: The imprint of tropical tropopause  
743 temperatures on stratospheric water vapor. *J. Geophys. Res.*, **101**, 3989–4006.

744 Perlwitz, J., S. Pawson, R. Fogt, J. E. Nielsen, and W. Neff, 2008: The impact of  
745 stratospheric ozone hole recovery on antarctic climate. *Geophys. Res. Lett.*, **35**, L08 714,  
746 doi:10.1029/2008GL033 317.

747 Plumb, R. A., 2002: Stratospheric transport. *J. Meteor. Soc. Japan*, **80**, 793–809.

748 Polvani, L. M. and P. J. Kushner, 2002: Tropospheric response to stratospheric pertur-  
749 bations in a relatively simple general circulation model. *Geophys. Res. Lett.*, **29** (7),  
750 10.1029/2001GL014 284.

751 Polvani, L. M., D. W. Waugh, G. J. P. Correa, and S.-W. Son, 2011: Stratospheric ozone de-  
752 pletion: the main driver of 20th Century atmospheric circulation changes in the Southern  
753 Hemisphere. *J. Climate*, in press.

754 Rosenlof, K. H., 1995: Seasonal cycle of the residual mean meridional circulation in the  
755 stratosphere. *J. Geophys. Res.*, **100**, 5173–5191.

756 Shaw, T. A., M. Sigmond, T. G. Shepherd, and J. F. Scinocca, 2009: Sensitivity of simulated  
757 climate to conservation of momentum in gravity wave drag parameterization. *J. Climate*,  
758 **22**, 2726–2742.

759 Shepherd, T. G. and T. A. Shaw, 2004: The angular momentum constraint on climate  
760 sensitivity and downward influence in the middle atmosphere. *J. Atmos. Sci.*, **61**, 2899–  
761 2908.

- 762 Simpson, I. R., M. Blackburn, and J. D. Haigh, 2009: The role of eddies in driving the  
763 tropospheric response to stratospheric heating perturbations. *J. Atmos. Sci.*, **66**, 1347–  
764 1365, doi:10.1175/2008JAS2758.1.
- 765 Sobel, A. and R. A. Plumb, 1999: Quantitative diagnostics of mixing in a shallow water  
766 model of the stratosphere. *J. Atmos. Sci.*, **56**, 2811–2829.
- 767 Solomon, S., K. H. Rosenlof, R. W. Portmann, J. S. Daniel, S. M. Davis, T. J. Sanford, and  
768 G.-K. Plattner, 2010: Contributions of stratospheric water vapor to decadal changes in  
769 the rate of global warming. *Science*, **327**, 1219–1223.
- 770 Son, S.-W., et al., 2008: The impact of stratospheric ozone recovery on the Southern Hemi-  
771 sphere westerly jet. *Science*, **320**, 1486–1489, doi: 10.1126/science.1155939.
- 772 Thompson, D. W. J. and S. Solomon, 2002: Interpretation of recent southern hemisphere  
773 climate change. *Science*, **296**, 895–899.
- 774 Vallis, G. K., 2006: *Atmospheric and Oceanic Fluid Dynamics*. Cambridge University Press,  
775 Cambridge, U.K., 745 pp.
- 776 Waugh, D. W. and T. M. Hall, 2002: Age of stratospheric air: Theory, observations, and  
777 models. *Rev. Geophys.*, **40**, 1010, doi:10.1029/2000RG000101.
- 778 Yulaeva, E., J. R. Holton, and J. M. Wallace, 1994: On the cause of the annual cycle in  
779 tropical lower-stratospheric temperatures. *J. Atmos. Sci.*, **51**, 169–174.

## 780 **List of Tables**

781 1 Details of the integrations presented in this study. We have grouped the inte-  
782 grations into different parameter sweep experiments; thus a few integrations  
783 have been listed multiple times for clarity. In the last column, we highlight  
784 which figure the simulation has been presented. Note that all integrations are  
785 used in Figs. 11 and 12. 33

TABLE 1. Details of the integrations presented in this study. We have grouped the integrations into different parameter sweep experiments; thus a few integrations have been listed multiple times for clarity. In the last column, we highlight which figure the simulation has been presented. Note that all integrations are used in Figs. 11 and 12.

$N$	$\gamma$ (K km <sup>-1</sup> )	$k$	$h_0$ (km)	Figures
1	4	-	0	1-5,8,10,13-15
2	4	2	1	4-7,10,14-16
3	4	2	2	4-6,10,14-15
4	4	2	3	4-6,10,14-15
5	4	2	4	1-8,10,13-15
6	4	1	1	6,8
7	4	1	2	6,8
8	4	1	3	6,8
9	4	1	4	6,8
10	4	1	5	6,8
9	4	1	4	[see above]
5	4	2	4	[see above]
11	4	3	4	8
12	4	4	4	8
13	0	2	3	4-6,9,10,14-15
14	1	2	3	4-6,10,14-15
15	1.5	2	3	1-3,13
16	2	2	3	4-6,9,10,14-16
17	3	2	3	4-6,10,14-15
4	4	2	3	[see above]
18	5	2	3	1-6,10,13-15
19	6	2	3	4-6,9,10,14-15
20	0	-	0	8
21	2	-	0	8
1	4	-	0	[see above]
22	6	-	0	8

## 786 List of Figures

- 787 1 The mean age of air in four integrations of the idealized model, contrasting two  
788 with a very “old” stratosphere at the top (a,b) and two with a very “young”  
789 stratospheres at the bottom (c,d). The two integrations on the left (a,c) differ  
790 only in the surface topography, while those on the right (b,d) differ only in  
791 the strength of the vortex lapse rate parameter  $\gamma$ . The age is shown relative  
792 to air entering the stratosphere at 100 hPa. Wave number 2 topography was  
793 used in all integrations, and panels a-d correspond to integrations 1, 15, 5,  
794 and 18, respectively. 38
- 795 2 The same as Fig. 1, but now plotting the time and zonal mean zonal wind,  $\bar{u}$ .  
796 Note that the vertical axis has been changed to show the troposphere as well. 39
- 797 3 The same as Fig. 1, but now plotting the residual mean mass streamfunction  
798  $\psi^*$ . The contour interval is  $0.5\text{e}9 \text{ kg s}^{-1}$ , except that we have included contours  
799 at  $\pm 0.25\text{e}9 \text{ kg s}^{-1}$  to highlight the circulation in the upper stratosphere. The  
800 zero contour is bold. 40
- 801 4 The residual mean pressure velocity  $\bar{\omega}^*$  at top (a,b) 10 and bottom (c,d) 100  
802 hPa. In the left panels (a,c), the integrations differ only in the amplitude  $h_0$  of  
803 wavenumber 2 topography at the surface, and the vortex lapse rate parameter  
804  $\gamma$  is fixed at  $4 \text{ K km}^{-1}$ . In the right column (b,d), the surface topography is  
805 fixed, with wavenumber  $k=2$  and amplitude  $h_0=3 \text{ km}$ , and  $\gamma$  is varied. Note  
806 that while topography has a similar impact on the circulation at both levels,  
807 the vortex strength has the opposite impact at 10 and 100 hPa. 41

- 808 5 The vertical structure of the residual circulation and wave driving. At top,  
809 the total downward mass flux as a function of height for integrations in which  
810 the (a) topography and (b) cooling of the polar vortex are varied. The sign  
811 of the mass transport is reversed in the Northern Hemisphere for clarity, so  
812 that the total transport by the residual circulation at each pressure level is the  
813 horizontal distances between the curves. Panels (c,d) show the total integrated  
814 wave forcing from the top of the atmosphere to each pressure level,  $\tau$  from  
815 equation (5), for the same integrations. Again, the sign is reversed in the  
816 NH. While the topography primarily controls the total amplitude of the wave  
817 driving, the vortex lapse rate  $\gamma$  controls its shape. 42
- 818 6 The root mean square (RMS) stationary wave amplitude at  $60^\circ\text{N}$ , as a func-  
819 tion of pressure, for integrations in which (a)  $h_0$  is varied for wavenumber 2  
820 topography and fixed  $\gamma = 4 \text{ K km}^{-1}$ , (b)  $\gamma$  is varied for integrations with fixed  
821 wavenumber 2 topography of amplitude  $h_0=3 \text{ km}$ , and (c) as in (a), but for  
822 wavenumber 1 topography. 43
- 823 7 The stationary wave structure at  $60^\circ\text{N}$  in two integrations with a cold vortex  
824 ( $\gamma = 4 \text{ K km}^{-1}$ ) and wavenumber 2 topography of amplitude (a) 1 and (b) 4  
825 km. 44
- 826 8 The total integrated wave forcing from the top of the atmosphere to each  
827 pressure level, as shown in Fig. 5c and d, but for integrations in which (a) the  
828 amplitude  $h_0$  of wavenumber 1 topography is varied,  $\gamma$  fixed at  $4 \text{ K km}^{-1}$ , (b)  
829 the wavenumber  $k$  of the topography is varied,  $h_0$  and  $\gamma$  fixed at 4 km and 4  
830  $\text{K km}^{-1}$ , respectively, and (c)  $\gamma$  is varied with a flat lower boundary. 45

- 831 9 The stratospheric wave guide for three integrations with varying polar vor-  
832 tex strength. On the right (a,c,e) the potential vorticity gradient  $\partial\bar{q}/\partial y$  is  
833 shaded in color (in units of  $\beta$  at  $45^\circ\text{N}$ ) and the zonal mean wind is denoted by  
834 black contours (only positive winds are shown, the zero contour in bold, and  
835 the contour interval is  $10 \text{ ms}^{-1}$ ). On the left (b,d,f) the index of refraction  
836 is shown in color shading and the divergence of the E-P flux in black con-  
837 tours (only negative values are shown and the thin/thick contour interval is  
838  $0.5/1.5 \text{ ms}^{-1}\text{day}^{-1}$ ). All three integrations have wavenumber 2 topography  
839 of amplitude  $h_0 = 3 \text{ km}$ , and  $\gamma$  is (a,b) 0, (c,d) 2, and (e,f)  $6 \text{ K km}^{-1}$ . 46
- 840 10 Changes in (a,b) the mean age of air at the equator and (c,d) the total tropical  
841 upwelling as a function of (a,c) the amplitude  $h_0$  of wavenumber 2 topography  
842 with fixed vortex strength  $\gamma = 4 \text{ K km}^{-1}$  and (b,d) vortex strength  $\gamma$  with  
843 fixed topography ( $k=2, h_0=3$ ). Note the use of two vertical axes in the lower  
844 plots. 47
- 845 11 Scatter plots showing the relationship between the mean age of air at the  
846 equator, 10 hPa and the residual mean velocity  $\bar{\omega}^*$  at the equator and (a) 100  
847 hPa and (b) 28 hPa. The blue and red symbols highlight the integrations in  
848 which  $h_0$  and  $\gamma$  are varied, respectively, as shown in Fig. 10. 48
- 849 12 Correlation across all integrations between the mean age at the equator and  
850 10 hPa and the residual mean velocities (a)  $\bar{\omega}^*$  and (b)  $\bar{v}^*$  as a function of  
851 pressure and height. The black contours denote regions where  $R > 0.95$ . The  
852 mean age at 10 hPa and the equator (denoted by the white diamonds) is  
853 representative of age in the mid to upper stratosphere. 49

- 854 13 Properties of the age spectrum and mean age for the four integrations shown  
855 in Figs. 1-3. The two upper rows correspond to the “old” integrations and  
856 two lower rows to the “young” integrations. The left column shows the width  
857 of the age spectrum  $\Delta$ , the center column the modal age, and right column  
858 the meridional gradient of the mean age. 50
- 859 14 The impact of (a) topographic amplitude  $h_0$  and (c) vortex strength  $\gamma$  on the  
860 location of the tropopause. Panels (b) and (d) highlight the changes. In (a)  
861 and (b), all integrations have wavenumber 2 topography with fixed  $\gamma = 4$   
862  $\text{K km}^{-1}$ . In (c) and (d), the topography is fixed, with wavenumber 2 and  
863 amplitude  $h_0=3$  km. 51
- 864 15 The impact of (a) topographic amplitude  $h_0$  and (b) vortex strength  $\gamma$  on the  
865 temperature and location of the cold point. The cold point is defined by the  
866 minimum temperature in the tropics, averaged between  $10^\circ\text{S}$  and  $\text{N}$ . 52
- 867 16 The potential for structural change in the Brewer-Dobson Circulation. The  
868 difference in (a) the residual mean mass streamfunction,  $\psi^*$ , and (b) the mean  
869 age of air, between integrations 16 and 3, showing the impact of increasing the  
870 stationary wave forcing (increasing  $h_0$  from 2 to 3 km) while simultaneously  
871 warming the polar vortex (reducing  $\gamma$  from 4 to  $2 \text{ K km}^{-1}$ ). With coordinated  
872 changes in the forcing, it is possible to increase the circulation at lower levels  
873 while increasing the age at upper levels. 53

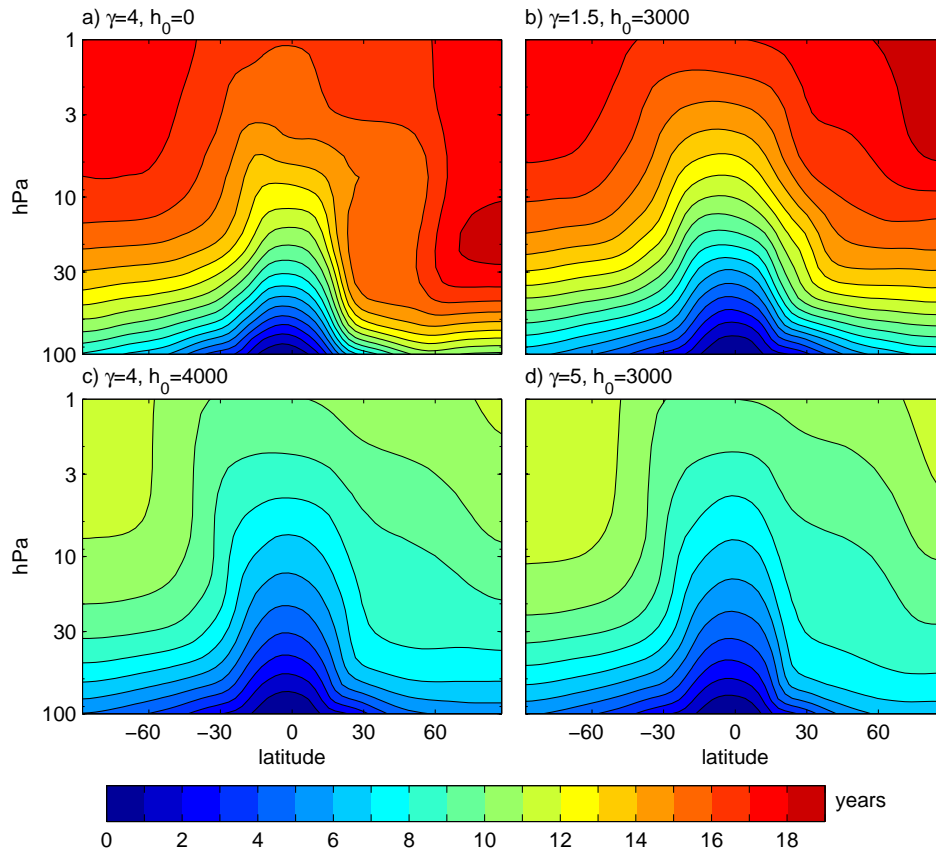


FIG. 1. The mean age of air in four integrations of the idealized model, contrasting two with a very “old” stratosphere at the top (a,b) and two with a very “young” stratospheres at the bottom (c,d). The two integrations on the left (a,c) differ only in the surface topography, while those on the right (b,d) differ only in the strength of the vortex lapse rate parameter  $\gamma$ . The age is shown relative to air entering the stratosphere at 100 hPa. Wave number 2 topography was used in all integrations, and panels a-d correspond to integrations 1, 15, 5, and 18, respectively.

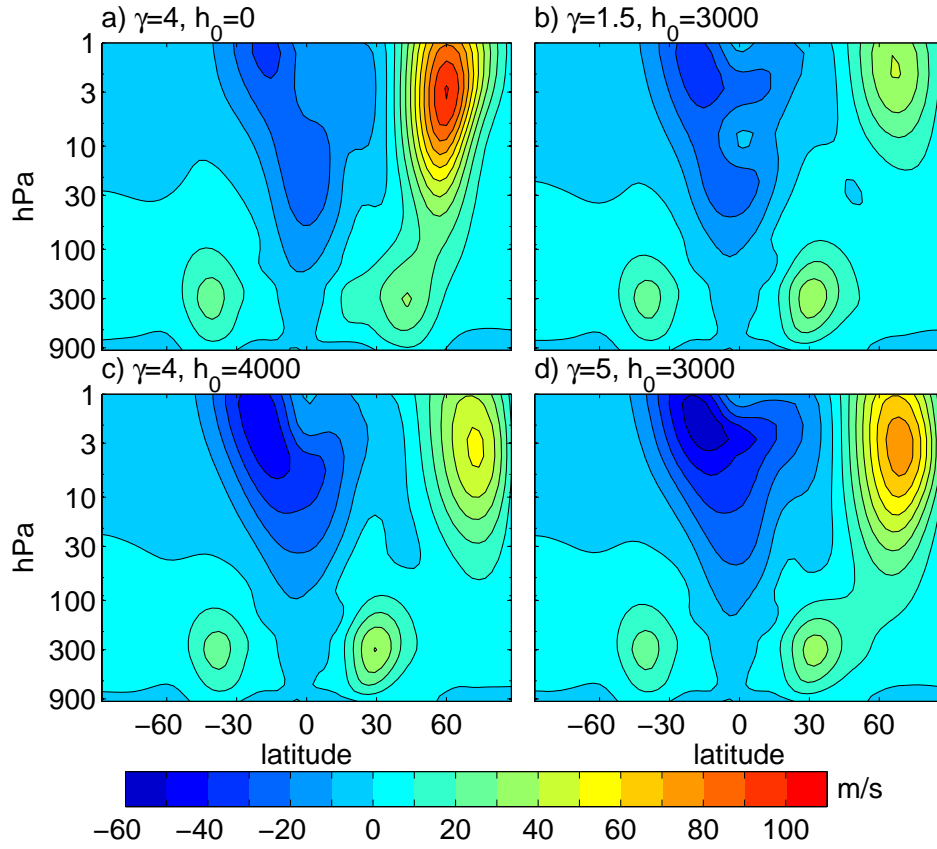


FIG. 2. The same as Fig. 1, but now plotting the time and zonal mean zonal wind,  $\bar{u}$ . Note that the vertical axis has been changed to show the troposphere as well.

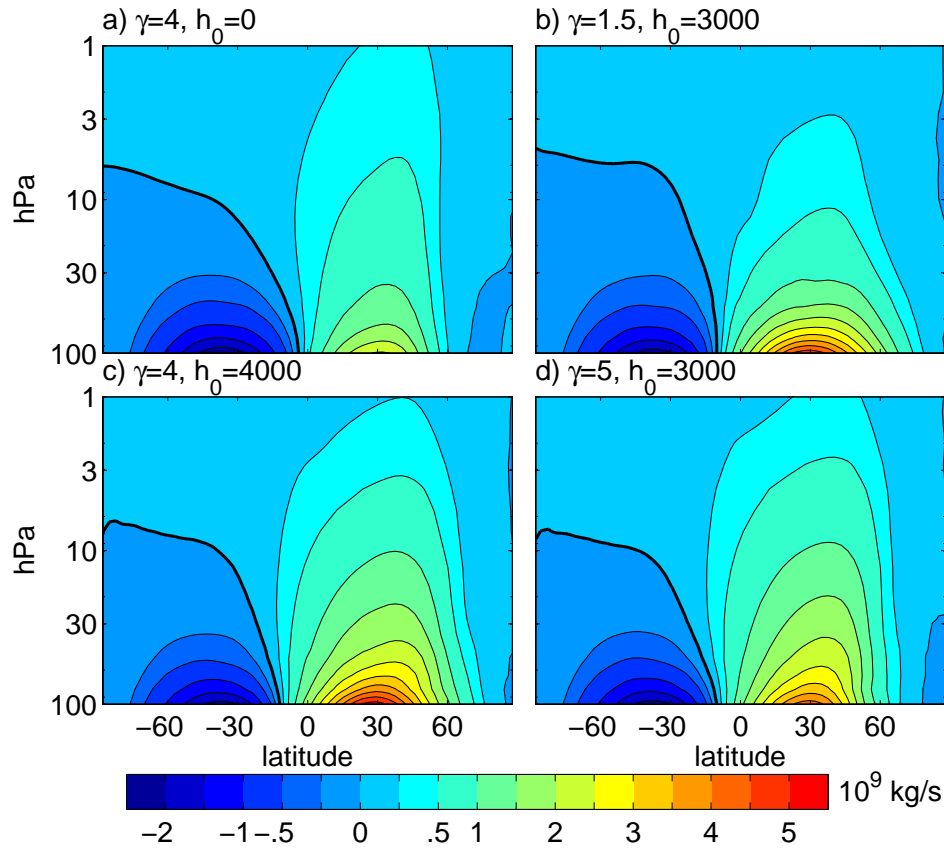


FIG. 3. The same as Fig. 1, but now plotting the residual mean mass streamfunction  $\psi^*$ . The contour interval is  $0.5e9 \text{ kg s}^{-1}$ , except that we have included contours at  $\pm 0.25e9 \text{ kg s}^{-1}$  to highlight the circulation in the upper stratosphere. The zero contour is bold.

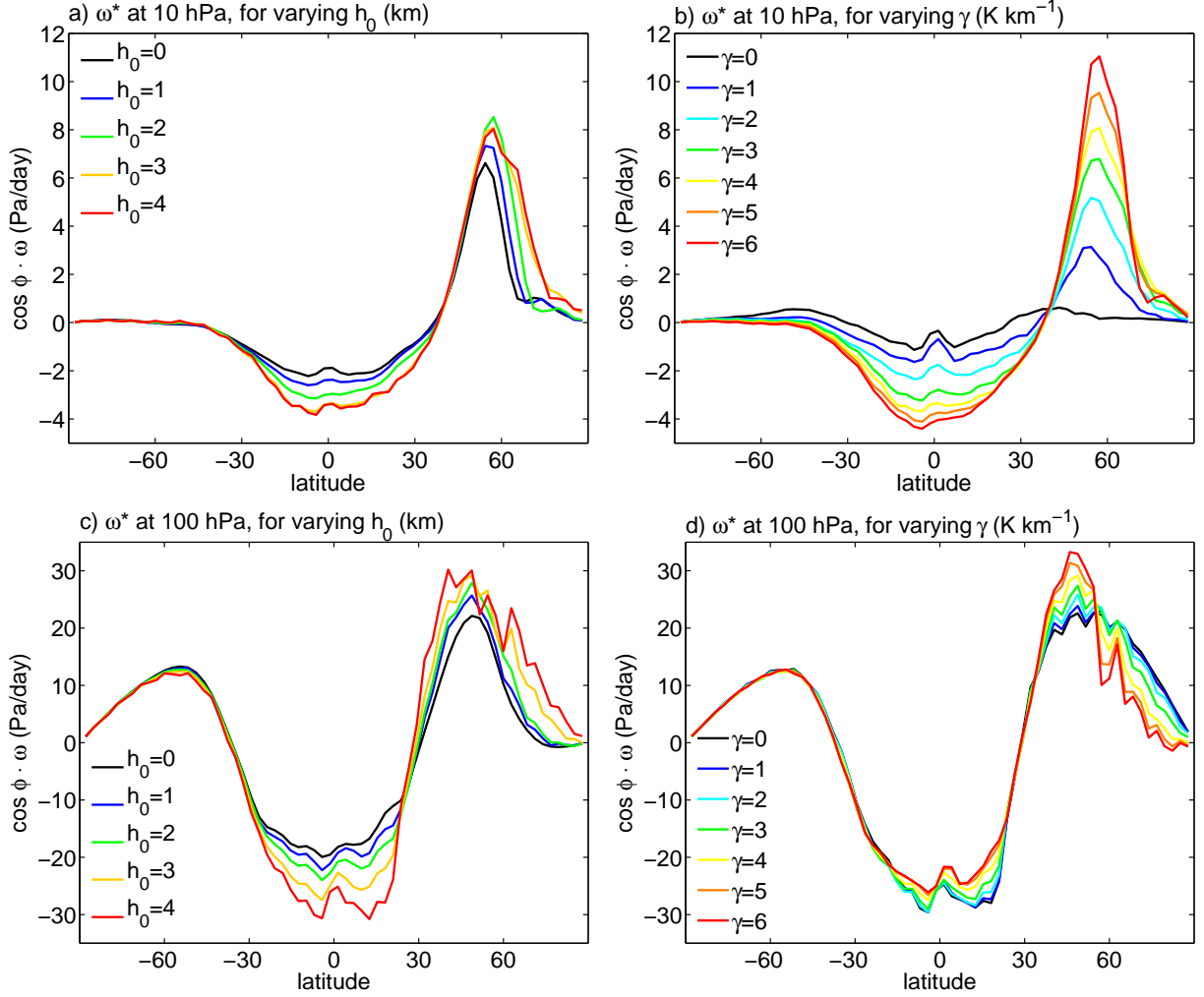


FIG. 4. The residual mean pressure velocity  $\overline{\omega}^*$  at top (a,b) 10 and bottom (c,d) 100 hPa. In the left panels (a,c), the integrations differ only in the amplitude  $h_0$  of wavenumber 2 topography at the surface, and the vortex lapse rate parameter  $\gamma$  is fixed at  $4 \text{ K km}^{-1}$ . In the right column (b,d), the surface topography is fixed, with wavenumber  $k=2$  and amplitude  $h_0=3 \text{ km}$ , and  $\gamma$  is varied. Note that while topography has a similar impact on the circulation at both levels, the vortex strength has the opposite impact at 10 and 100 hPa.

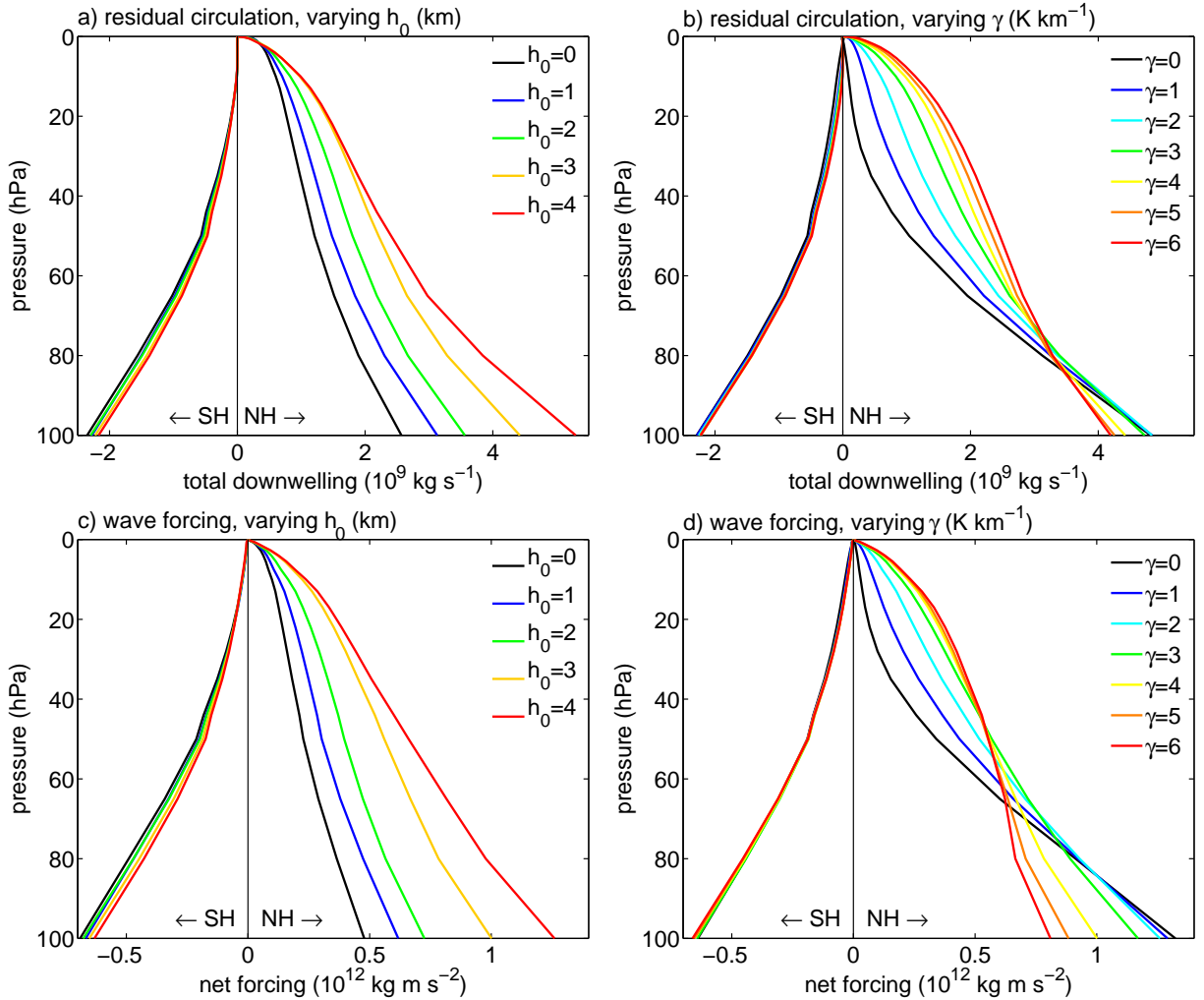


FIG. 5. The vertical structure of the residual circulation and wave driving. At top, the total downward mass flux as a function of height for integrations in which the (a) topography and (b) cooling of the polar vortex are varied. The sign of the mass transport is reversed in the Northern Hemisphere for clarity, so that the total transport by the residual circulation at each pressure level is the horizontal distances between the curves. Panels (c,d) show the total integrated wave forcing from the top of the atmosphere to each pressure level,  $\tau$  from equation (5), for the same integrations. Again, the sign is reversed in the NH. While the topography primarily controls the total amplitude of the wave driving, the vortex lapse rate  $\gamma$  controls its shape.

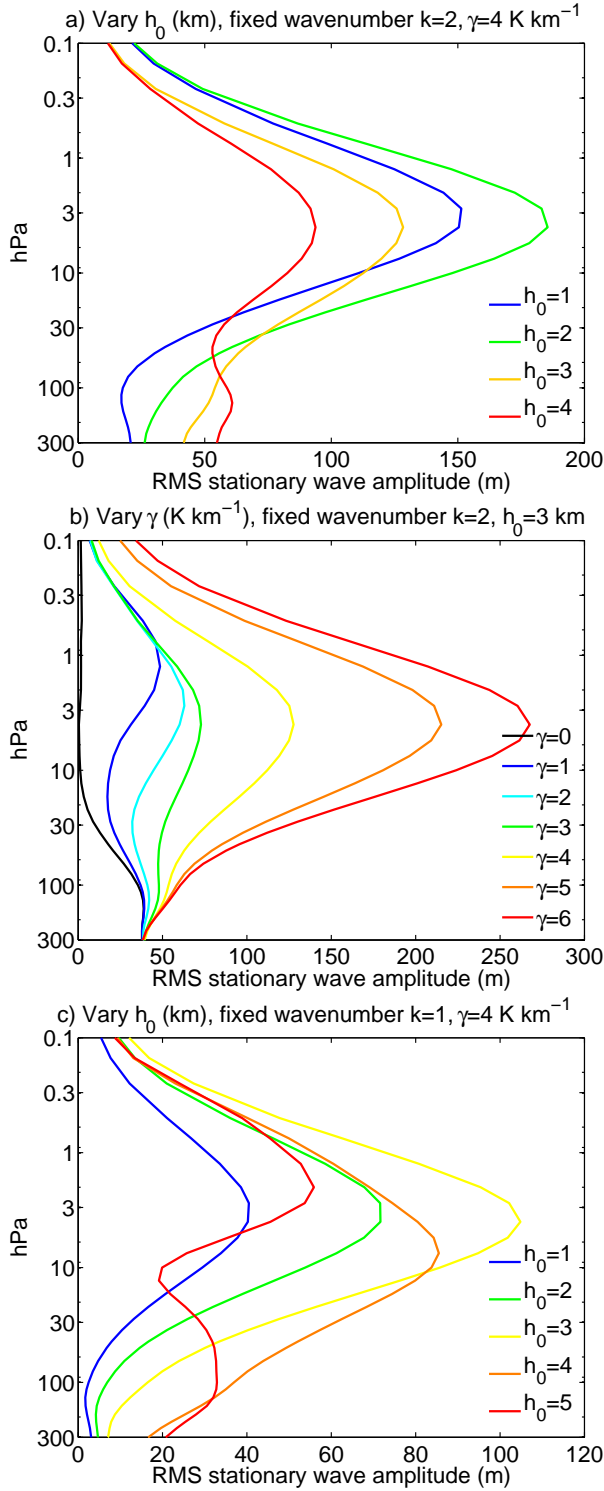


FIG. 6. The root mean square (RMS) stationary wave amplitude at  $60^\circ\text{N}$ , as a function of pressure, for integrations in which (a)  $h_0$  is varied for wavenumber 2 topography and fixed  $\gamma = 4 \text{ K km}^{-1}$ , (b)  $\gamma$  is varied for integrations with fixed wavenumber 2 topography of amplitude  $h_0=3 \text{ km}$ , and (c) as in (a), but for wavenumber 1 topography.

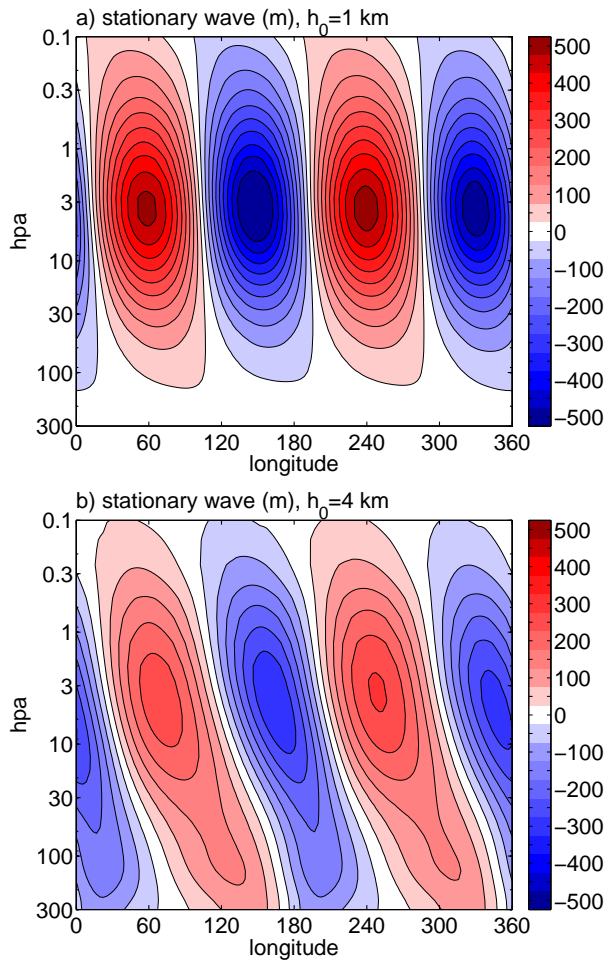


FIG. 7. The stationary wave structure at  $60^\circ\text{N}$  in two integrations with a cold vortex ( $\gamma = 4 \text{ K km}^{-1}$ ) and wavenumber 2 topography of amplitude (a) 1 and (b) 4 km.

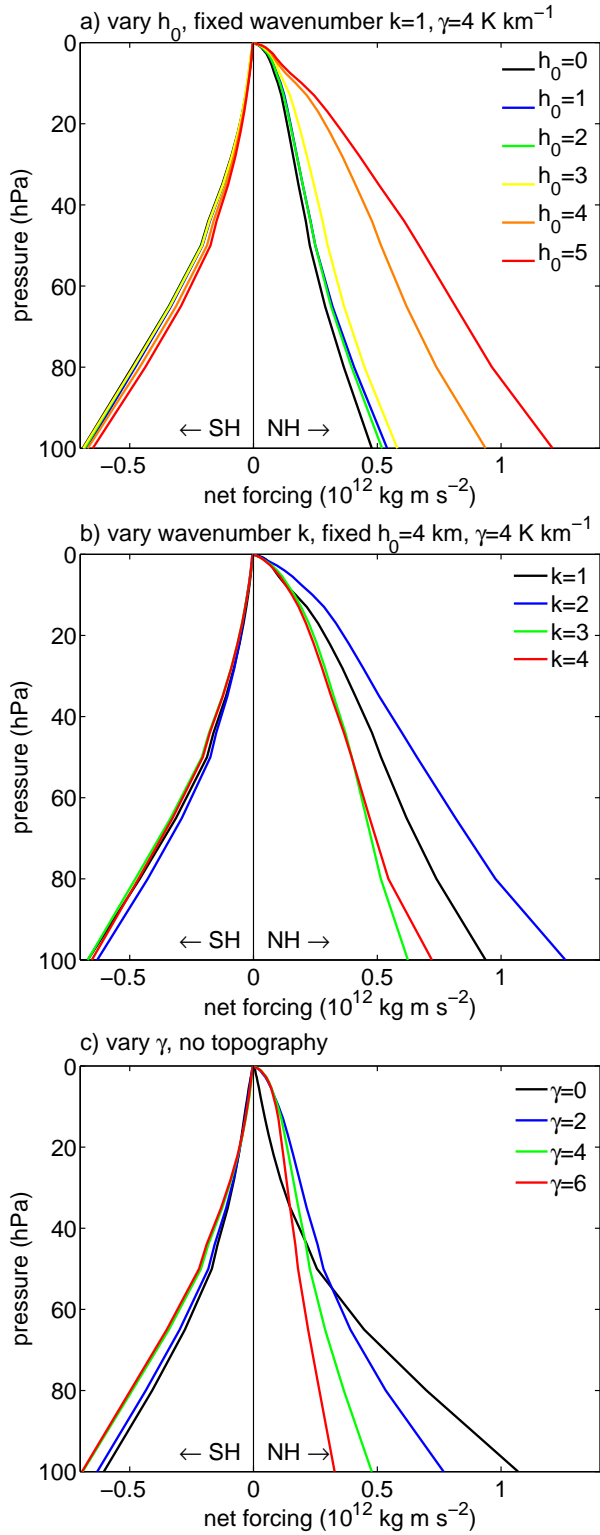


FIG. 8. The total integrated wave forcing from the top of the atmosphere to each pressure level, as shown in Fig. 5c and d, but for integrations in which (a) the amplitude  $h_0$  of wavenumber 1 topography is varied,  $\gamma$  fixed at  $4 \text{ K km}^{-1}$ , (b) the wavenumber  $k$  of the topography is varied,  $h_0$  and  $\gamma$  fixed at  $4 \text{ km}$  and  $4 \text{ K km}^{-1}$ , respectively, and (c)  $\gamma$  is varied with a flat lower boundary.

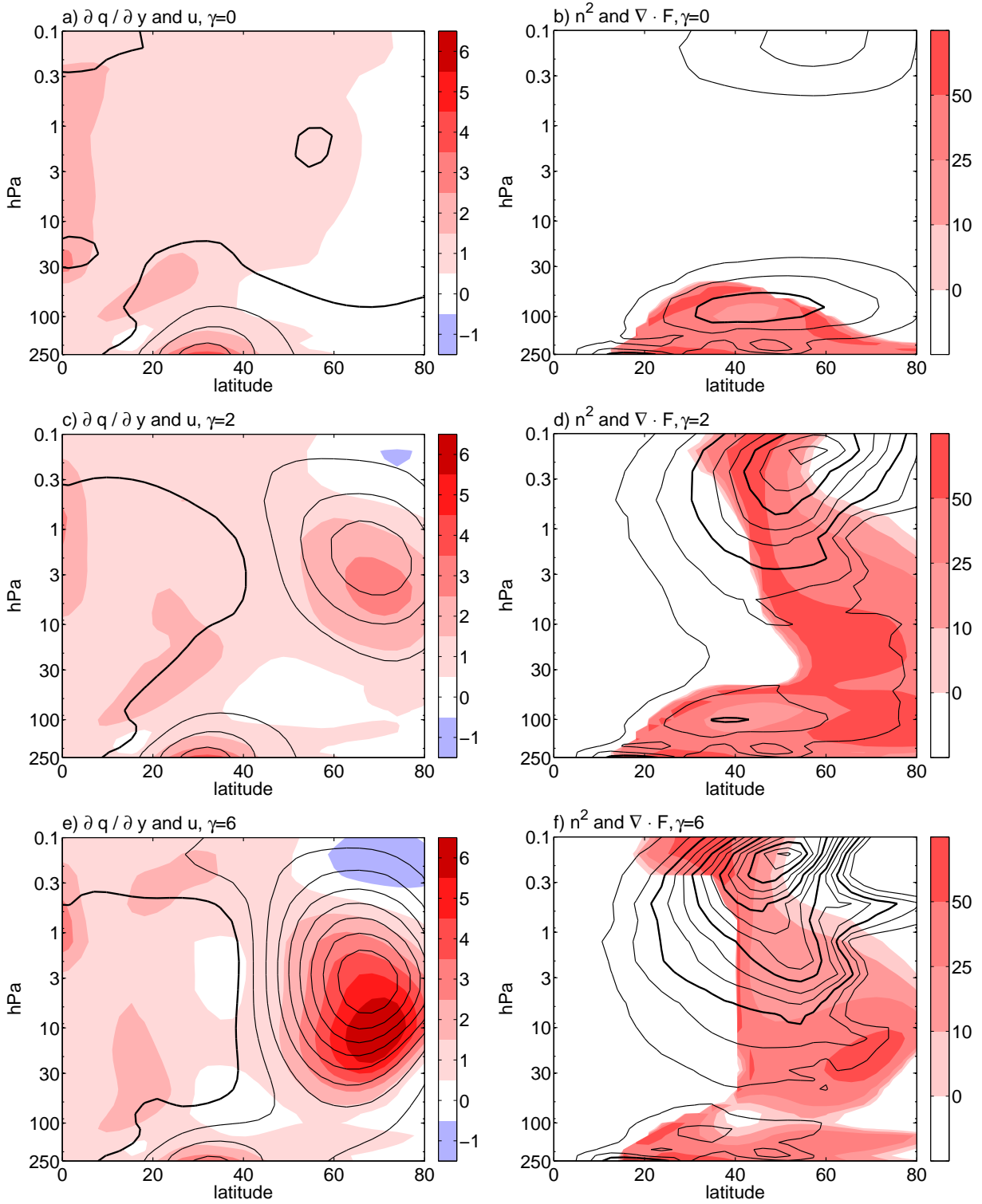


FIG. 9. The stratospheric wave guide for three integrations with varying polar vortex strength. On the right (a,c,e) the potential vorticity gradient  $\partial \bar{q} / \partial y$  is shaded in color (in units of  $\beta$  at  $45^\circ\text{N}$ ) and the zonal mean wind is denoted by black contours (only positive winds are shown, the zero contour in bold, and the contour interval is  $10 \text{ ms}^{-1}$ ). On the left (b,d,f) the index of refraction is shown in color shading and the divergence of the E-P flux in black contours (only negative values are shown and the thin/thick contour interval is  $0.5/1.5 \text{ ms}^{-1}\text{day}^{-1}$ ). All three integrations have wavenumber 2 topography of amplitude  $h_0 = 3 \text{ km}$ , and  $\gamma$  is (a,b) 0, (c,d) 2, and (e,f)  $6 \text{ K km}^{-1}$ .

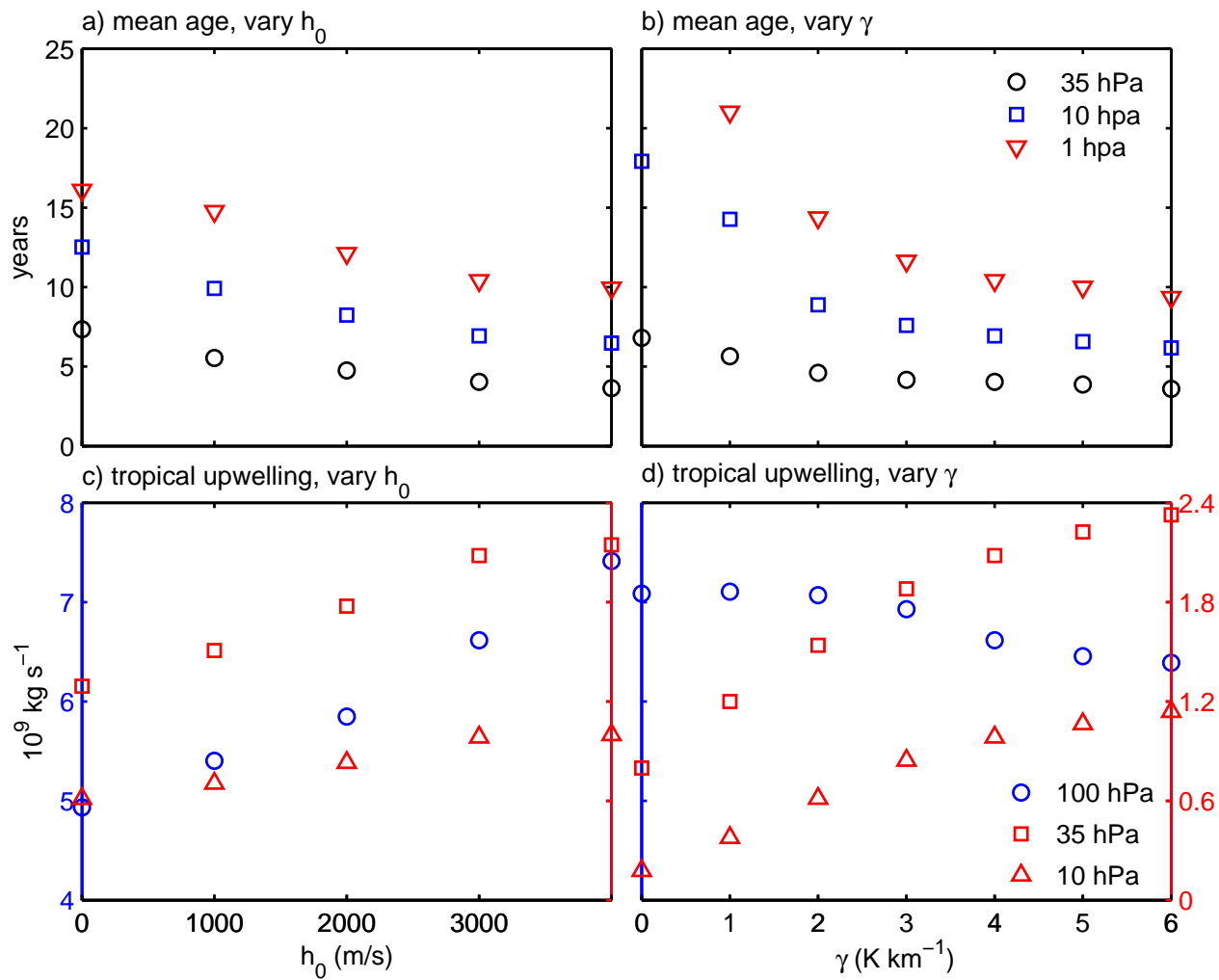


FIG. 10. Changes in (a,b) the mean age of air at the equator and (c,d) the total tropical upwelling as a function of (a,c) the amplitude  $h_0$  of wavenumber 2 topography with fixed vortex strength  $\gamma = 4 \text{ K km}^{-1}$  and (b,d) vortex strength  $\gamma$  with fixed topography ( $k=2$ ,  $h_0=3$ ). Note the use of two vertical axes in the lower plots.

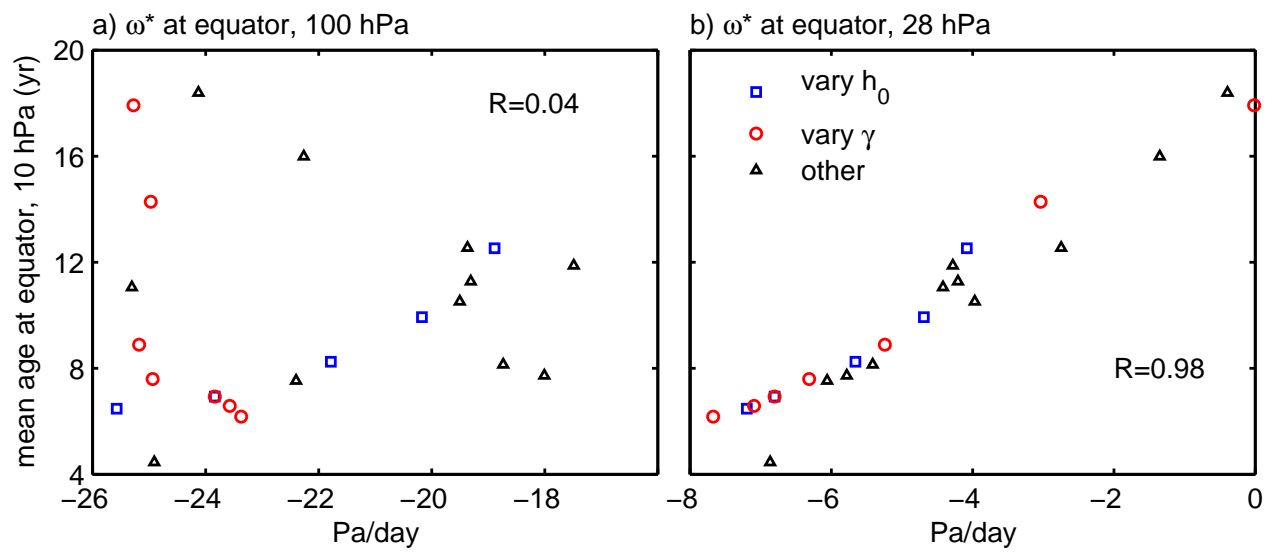


FIG. 11. Scatter plots showing the relationship between the mean age of air at the equator, 10 hPa and the residual mean velocity  $\bar{\omega}^*$  at the equator and (a) 100 hPa and (b) 28 hPa. The blue and red symbols highlight the integrations in which  $h_0$  and  $\gamma$  are varied, respectively, as shown in Fig. 10.

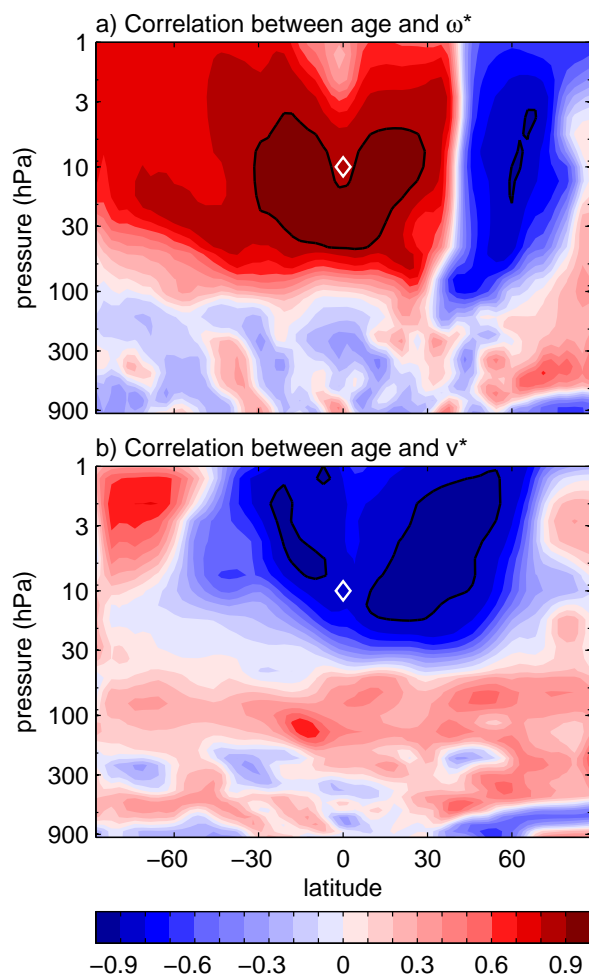


FIG. 12. Correlation across all integrations between the mean age at the equator and 10 hPa and the residual mean velocities (a)  $\overline{\omega}^*$  and (b)  $\overline{v}^*$  as a function of pressure and height. The black contours denote regions where  $R > 0.95$ . The mean age at 10 hPa and the equator (denoted by the white diamonds) is representative of age in the mid to upper stratosphere.

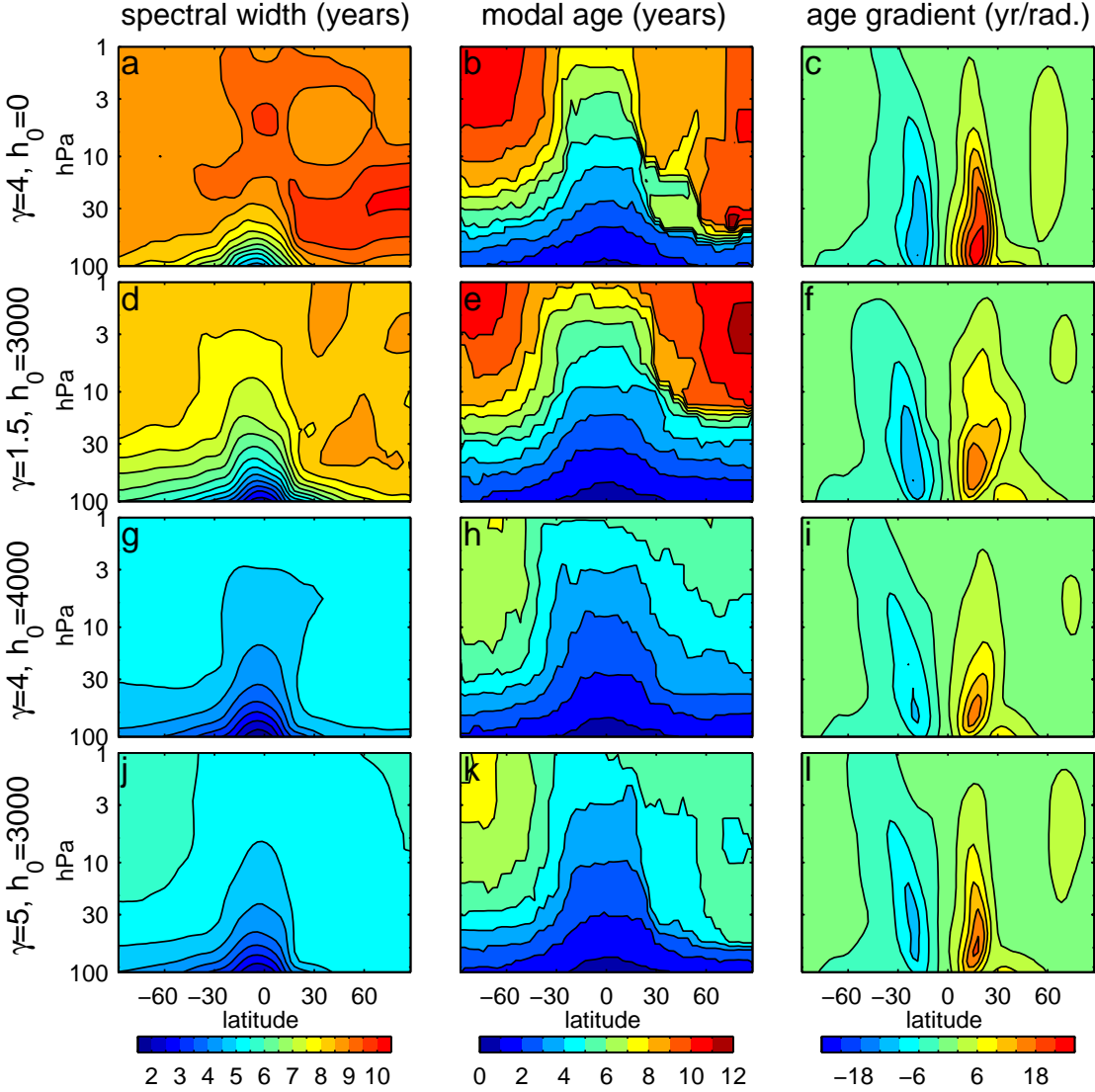


FIG. 13. Properties of the age spectrum and mean age for the four integrations shown in Figs. 1-3. The two upper rows correspond to the “old” integrations and two lower rows to the “young” integrations. The left column shows the width of the age spectrum  $\Delta$ , the center column the modal age, and right column the meridional gradient of the mean age.

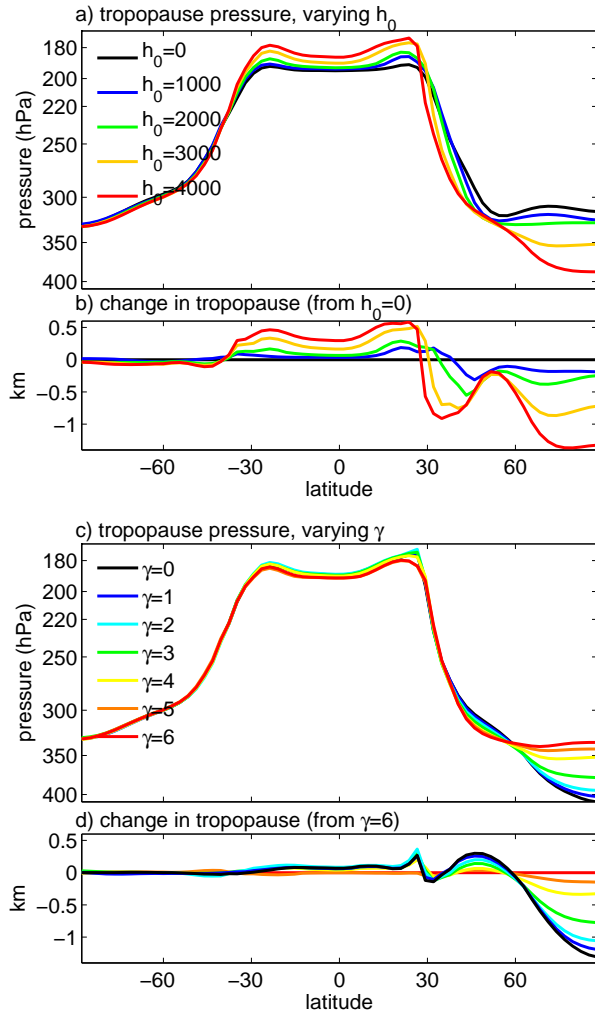


FIG. 14. The impact of (a) topographic amplitude  $h_0$  and (c) vortex strength  $\gamma$  on the location of the tropopause. Panels (b) and (d) highlight the changes. In (a) and (b), all integrations have wavenumber 2 topography with fixed  $\gamma = 4 \text{ K km}^{-1}$ . In (c) and (d), the topography is fixed, with wavenumber 2 and amplitude  $h_0=3 \text{ km}$ .

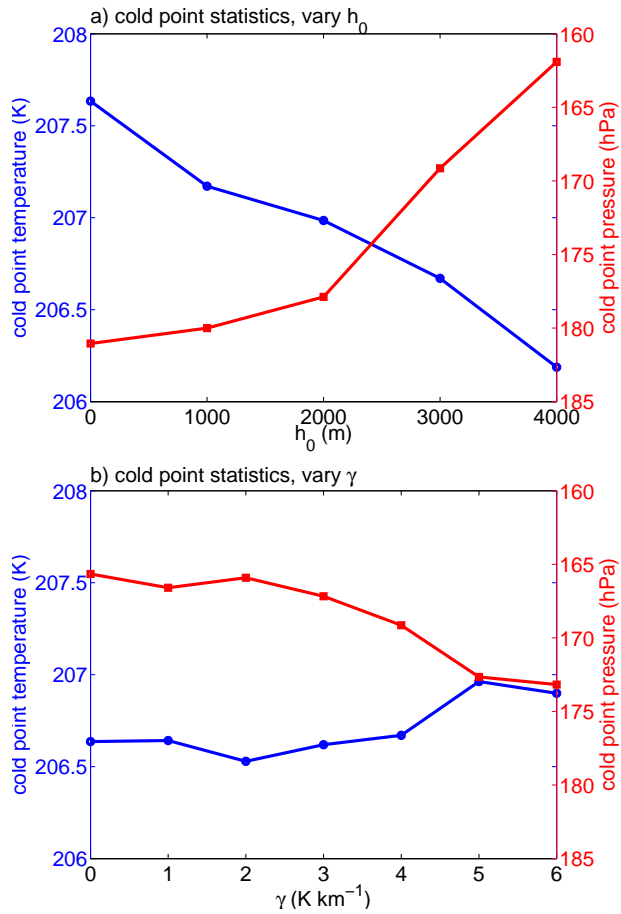


FIG. 15. The impact of (a) topographic amplitude  $h_0$  and (b) vortex strength  $\gamma$  on the temperature and location of the cold point. The cold point is defined by the minimum temperature in the tropics, averaged between  $10^\circ\text{S}$  and N.

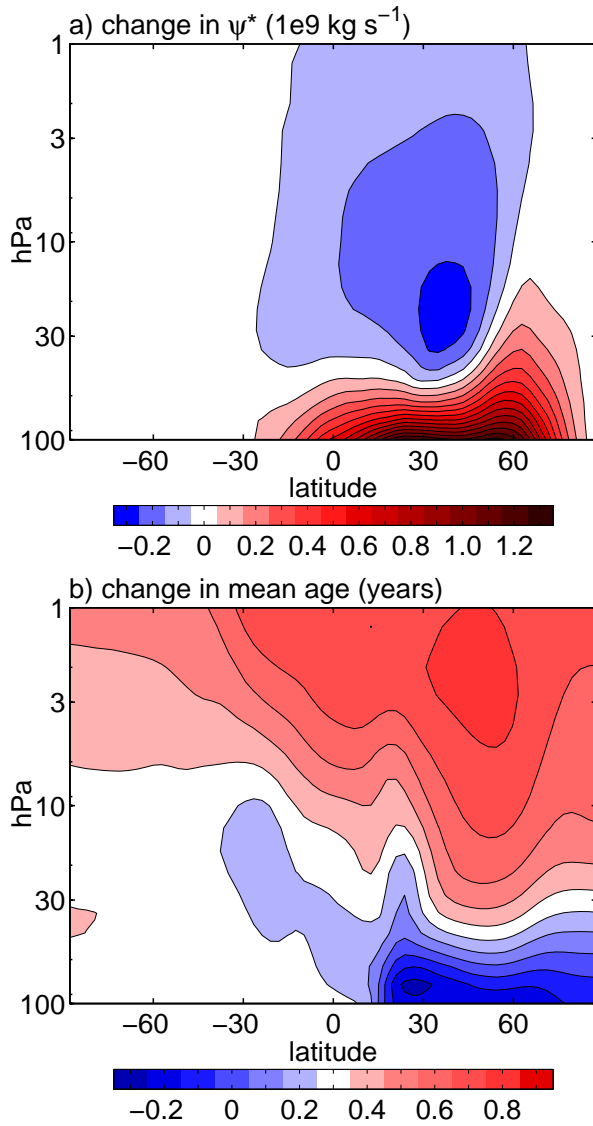


FIG. 16. The potential for structural change in the Brewer-Dobson Circulation. The difference in (a) the residual mean mass streamfunction,  $\psi^*$ , and (b) the mean age of air, between integrations 16 and 3, showing the impact of increasing the stationary wave forcing (increasing  $h_0$  from 2 to 3 km) while simultaneously warming the polar vortex (reducing  $\gamma$  from 4 to 2  $\text{K km}^{-1}$ ). With coordinated changes in the forcing, it is possible to increase the circulation at lower levels while increasing the age at upper levels.